

# Measuring the Charged Pion Polarizability in the $\gamma\gamma \rightarrow \pi^+\pi^-$ Reaction

(A proposal to the 40<sup>th</sup> Jefferson Lab Program Advisory Committee)

A. AlekSejevs<sup>1</sup>, S. Barkanova<sup>1</sup>, M. Dugger<sup>2</sup>, B. Ritchie<sup>2</sup>, I. Senderovich<sup>2</sup>, E. Anassontzis<sup>3</sup>, P. Ioannou<sup>3</sup>, C. Kourkouveli<sup>3</sup>, G. Voulgaris<sup>3</sup>, N. Jarvis<sup>4</sup>, W. Levine<sup>4</sup>, P. Mattione<sup>4</sup>, W. McGinley<sup>4</sup>, C. A. Meyer<sup>4</sup>, R. Schumacher<sup>4</sup>, M. Staib<sup>4</sup>, P. Collins<sup>5</sup>, F. Klein<sup>5</sup>, D. Sober<sup>5</sup>, D. Doughty<sup>6</sup>, A. Barnes<sup>7</sup>, R. Jones<sup>7</sup>, J. McIntyre<sup>7</sup>, F. Mokaya<sup>7</sup>, B. Pratt<sup>7</sup>, W. Boeglin<sup>8</sup>, L. Guo<sup>8</sup>, P. Khetarpal<sup>8</sup>, E. Pooser<sup>8</sup>, J. Reinhold<sup>8</sup>, H. Al Ghoul<sup>9</sup>, S. Capstick<sup>9</sup>, V. Crede<sup>9</sup>, P. Eugenio<sup>9</sup>, A. Ostrovidov<sup>9</sup>, N. Sparks<sup>9</sup>, A. Tsaris<sup>9</sup>, D. Ireland<sup>10</sup>, K. Livingston<sup>10</sup>, D. Dale<sup>11</sup>, M. Khandaker<sup>11</sup>, D. Bennett<sup>12</sup>, J. Bennett<sup>12</sup>, J. Frye<sup>12</sup>, M. Lara<sup>12</sup>, J. Leckey<sup>12</sup>, R. Mitchell<sup>12</sup>, K. Moriya<sup>12</sup>, M. R. Shepherd<sup>12</sup>, A. Szczepaniak<sup>12</sup>, **R. Miskimen**<sup>\*13</sup>, A. Mushkarenkov<sup>13</sup>, A. Bernstein<sup>14</sup>, J. Hardin<sup>14</sup>, P. Martel<sup>14</sup>, J. Stevens<sup>14</sup>, M. Williams<sup>14</sup>, D. Hornidge<sup>15</sup>, A. Ponosov<sup>16</sup>, S. Somov<sup>16</sup>, C. Salgado<sup>17</sup>, P. Ambrozewicz<sup>18</sup>, A. Gasparian<sup>18</sup>, R. Pedroni<sup>18</sup>, T. Black<sup>19</sup>, L. Gan<sup>19</sup>, S. Dobbs<sup>20</sup>, K. K. Seth<sup>20</sup>, A. Tomaradze<sup>20</sup>, F. Close<sup>21</sup>, E. Swanson<sup>22</sup>, S. Denisov<sup>23</sup>, G. Huber<sup>24</sup>, D. Kolybaba<sup>24</sup>, S. Krueger<sup>24</sup>, G. Lolos<sup>24</sup>, Z. Papandreou<sup>24</sup>, A. Semenov<sup>24</sup>, I. Semenova<sup>24</sup>, M. Tahani<sup>24</sup>, W. Brooks<sup>25</sup>, H. Hakobyan<sup>25</sup>, S. Kuleshov<sup>25</sup>, O. Soto<sup>25</sup>, A. Toro<sup>25</sup>, I. Vega<sup>25</sup>, R. White<sup>25</sup>, F. Barbosa<sup>26</sup>, E. Chudakov<sup>†26</sup>, H. Egiyan<sup>26</sup>, M. Ito<sup>26</sup>, D. Lawrence<sup>26</sup>, D. Mack<sup>26</sup>, M. McCaughan<sup>26</sup>, M. Pennington<sup>26</sup>, L. Pentchev<sup>26</sup>, Y. Qiang<sup>26</sup>, E. S. Smith<sup>26</sup>, A. Somov<sup>26</sup>, S. Taylor<sup>26</sup>, T. Whitlatch<sup>26</sup>, E. Wolin<sup>26</sup>, and B. Zihlmann<sup>26</sup>

<sup>1</sup>*Acadia University, Wolfville, Nova Scotia, Canada*

<sup>2</sup>*Arizona State University, Tempe, AZ*

<sup>3</sup>*University of Athens, Athens, Greece*

<sup>4</sup>*Carnegie Mellon University, Pittsburgh, PA*

<sup>5</sup>*Catholic University of America, Washington, D.C.*

<sup>6</sup>*Christopher Newport University, Newport News, VA*

<sup>7</sup>*University of Connecticut, Storrs, CT*

<sup>8</sup>*Florida International University, Miami, FL*

<sup>9</sup>*Florida State University, Tallahassee, FL*

<sup>10</sup>*University of Glasgow, Glasgow, United Kingdom*

<sup>11</sup>*Idaho State University, Pocatello, ID*

<sup>12</sup>*Indiana University, Bloomington, Indiana*

<sup>13</sup>*University of Massachusetts, Amherst, MA*

<sup>14</sup>*Massachusetts Institute of Technology, Cambridge, MA*

<sup>15</sup>*Mt. Allison University, Sackville, NB, Canada*

<sup>16</sup>*MEPHI, Moscow, Russia*

<sup>17</sup>*Norfolk State University, Norfolk, Virginia*

<sup>18</sup>*North Carolina A&T State University, Greensboro, NC*

<sup>19</sup>*University of North Carolina, Wilmington, NC*

<sup>20</sup>*Northwestern University, Evanston, IL*

<sup>21</sup>*University of Oxford, Oxford, United Kingdom*

<sup>22</sup>*University of Pittsburgh, Pittsburgh, PA*

<sup>23</sup>*Institute for High Energy Physics, Protvino, Russia*

<sup>24</sup>*University of Regina, Regina, SK, Canada*

<sup>25</sup>*Universidad Técnica Federico Santa María, Valparaíso, Chile*

<sup>26</sup>*Thomas Jefferson National Accelerator Facility, Newport News, VA*

---

\*Spokesperson and contact person

†Hall D Leader

## Abstract

This proposal presents our plan to make a precision measurement of the charged pion polarizability  $\alpha_\pi - \beta_\pi$  through measurements of  $\gamma\gamma \rightarrow \pi^+\pi^-$  cross sections using the GlueX detector in Hall D. The accuracy of the proposed measurement is estimated at 10%, with an absolute error in  $\alpha - \beta$  of  $\pm 0.6 \times 10^{-4} \text{ fm}^3$ . The charged pion polarizability ranks among the most important tests of low-energy QCD presently unresolved by experiment. A measurement of the pion polarizability tests fundamental symmetries in the intrinsic even-parity sector of QCD.

## 1 Introduction

Electromagnetic polarizabilities are fundamental properties of composite systems such as molecules, atoms, nuclei, and hadrons [Ho90]. Whereas magnetic moments provide information about the ground state properties of a system, polarizabilities provides information about the excited states of the system. For atomic systems polarizabilities are on the order of the atomic volume. For hadrons the polarizabilities are much smaller than the volume, typically of the order of  $10^{-4} \text{ fm}^3$ , because of the greater stiffness of the QCD force as compared to the electromagnetic force. Measurements of hadron polarizabilities provide an important test point for effective field theories, and dispersion and lattice calculations. Among the hadron polarizabilities, the charged pion polarizability ranks of paramount importance because it tests fundamental symmetries at leading order. The pion polarizability may also play a role in the  $(g - 2)_\mu$  anomaly; Ramsey-Musolf and collaborators have found that an omitted contribution to the hadronic light-by-light scattering contribution to  $(g - 2)_\mu$  from the pion polarizability is substantial and potentially significant [En12].

Hadron polarizabilities are best measured in Compton scattering experiments, where in the case of nucleon polarizabilities, one looks for a deviation of the cross section from the prediction of Compton scattering from a structureless Dirac particle. Because a free pion target does not exist, the measurements to date of the charged pion polarizability have been plagued by experimental and theoretical uncertainties. This proposal presents a plan to make a precision measurement of the charged pion polarizability by measurement of  $\gamma\gamma \rightarrow \pi^+\pi^-$  cross sections using the GlueX detector in Hall D.

## 2 Theoretical predictions for the charged pion polarizability

Theory for the charged pion polarizability results directly from the original formulation of chiral perturbation theory (ChPT) by Gasser and Leutwyler [Ga84]. This Lagrangian is invariant under the transformation  $\phi_i \rightarrow -\phi_i$ , where  $\phi_i$  represents the eight Goldstone boson fields, and has the feature that it does not allow transitions between even and odd numbers of mesons. For example, the transition  $\pi^0 \rightarrow \gamma\gamma$  is not allowed at leading order  $O(p^4)$  [Ho92]. For this reason the Lagrangian must be augmented by the Wess-Zumino-Witten anomaly [We71]. Recently the PrimEx experiment at JLab made a precision test of the intrinsic odd-parity (anomalous) sector of low-energy QCD by measuring the radiative width for  $\pi^0 \rightarrow \gamma\gamma$  [La11]. A measurement of the charged pion polarizability probes the intrinsic even-parity sector of QCD.

The Partially Conserved Axial Current (PCAC) and leading order  $O(p^4)$  ChPT both predict that the electric and magnetic polarizabilities of the charged pion ( $\alpha_\pi$  and  $\beta_\pi$ ) are related to the charged pion weak form factors  $F_V$  and  $F_A$  in the decay  $\pi^+ \rightarrow e^+\nu\gamma$

$$\alpha_\pi = -\beta_\pi \times \frac{F_A}{F_V} = \frac{1}{6}(l_6 - l_5) \quad (1)$$

where  $l_5$  and  $l_6$  are low energy constants in the Gasser and Leutwyler effective Lagrangian [Ga84]. Using recent results from the PIBETA collaboration for  $F_A$  and  $F_V$  [By09], the  $O(p^4)$  ChPT prediction for the charged pion electric and magnetic polarizabilities is given by

$$\alpha_\pi = -\beta_\pi = (2.78 \pm 0.1) \times 10^{-4} fm^3 \quad (2)$$

with the  $O(p^6)$  corrections predicted to be relatively small [Bu96,Ga06], giving

$$\alpha_\pi - \beta_\pi = (5.7 \pm 1.0) \times 10^{-4} fm^3 \quad (3)$$

$$\alpha_\pi + \beta_\pi = (0.16 \pm 0.1) \times 10^{-4} fm^3 \quad (4)$$

Dispersion relations have also been used to find  $\alpha_\pi$  and  $\beta_\pi$  with differing conclusions. Fitting  $\gamma\gamma \rightarrow \pi^+\pi^-$  data from threshold up to 2.5 GeV to fix the dispersion integrals, Fil'kov et. al. [Fi06] found that  $\alpha_\pi - \beta_\pi = 13.0_{-1.9}^{+2.6} \times 10^{-4} fm^3$  and  $\alpha_\pi + \beta_\pi = 0.18_{-0.02}^{+0.11} \times 10^{-4} fm^3$ , which is in disagreement with ChPT. However, Pasquini *et al.* [Pa08] examined the Fil'kov calculation in detail, and noted that the energy extrapolations used by Fil'kov below and above meson resonances leave considerable room for model dependence. When the basic requirements of dispersion relations are taken into account, Pasquini *et al.* found that dispersion relations predict

$$\alpha_\pi - \beta_\pi = 5.7 \times 10^{-4} fm^3, \quad (5)$$

which is in agreement with ChPT.

### 3 Previous Measurements of the Charged Pion Polarizability

Previous measurements of  $\alpha_\pi - \beta_\pi$  are plotted in Fig. 1, grouped by experiment type. The ChPT and dispersion model predictions are also shown in the figure. Three different experimental techniques have been utilized to measure  $\alpha_\pi$  and  $\beta_\pi$ :

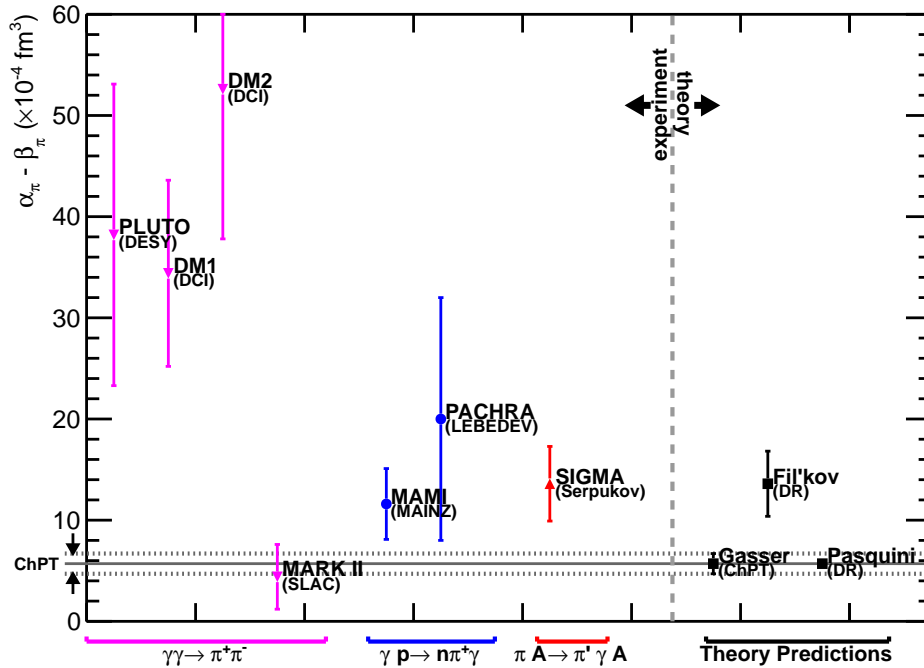


Figure 1: Experimental data for  $\alpha_\pi - \beta_\pi$  grouped by experiment type, and theoretical predictions

- Radiative pion photoproduction,  $\gamma p \rightarrow \gamma' \pi^+ n$ , at very low momentum transfer to the recoil nucleon. This reaction can be visualized as Compton scattering off a virtual pion. At forward Compton angles the reaction is sensitive to  $\alpha_\pi + \beta_\pi$ , and at backward angles,  $\alpha_\pi - \beta_\pi$ . The most recent measurement has been from

Mainz [Ah05]. Using the constraint  $\alpha_\pi = -\beta_\pi$  in their fits they obtained

$$\alpha_\pi - \beta_\pi = (11.6 \pm 1.5_{stat} \pm 3.0_{sys} \pm 0.5_{model}) \times 10^{-4} fm^3 \quad (6)$$

This result has attracted a great deal of attention in the field because of “disagreement” with ChPT. However, the measurement has limited statistical and systematic precision. When the statistical and systematic errors are combined in quadrature, the result differs only by  $1.7\sigma$  from the ChPT prediction.

- Primakoff effect of scattering a high energy pion in the Coulomb field of a heavy nucleus,  $\pi A \rightarrow \pi' \gamma A$ . This reaction is equivalent to the Compton scattering a nearly real photon off the pion. The most recent published measurement has been from Serpukov [An83]. Using the constraint  $\alpha_\pi = -\beta_\pi$ , they obtained

$$\alpha_\pi - \beta_\pi = (13.6 \pm 2.8_{stat} \pm 2.4_{sys}) \times 10^{-4} fm^3 \quad (7)$$

Combining errors in quadrature, this result differs by  $2.1\sigma$  from the ChPT prediction.

- $\gamma\gamma \rightarrow \pi^+\pi^-$ . By crossing symmetry (exchanging  $s$  and  $t$  variables in the scattering amplitude) the  $\gamma\gamma \rightarrow \pi\pi$  amplitude can be related to the  $\gamma\pi \rightarrow \gamma\pi$  amplitude. For the  $\gamma\gamma \rightarrow \pi\pi$  reaction, the sensitivity to the polarizabilities goes as  $\alpha_\pi - \beta_\pi$ . Babusci *et al.* [Ba92] used chiral perturbation theory with a one-loop correction to derive a formula which they used to obtain pion polarizabilities from  $\gamma\gamma \rightarrow \pi^+\pi^-$  data. Examining data sets from PLUTO, DM1, DM2, and MARK II, they obtained values of  $\alpha_\pi - \beta_\pi$  ranging from  $52.6 \pm 14.8_{stat}$  (from DM2) to  $4.4 \pm 3.2_{stat}$  (from MARK II).

It is difficult to draw conclusions from the present experimental results. It is generally recognized that the most model independent technique to measure hadron polarizabilities is through Compton scattering. However, the two most recent Compton measurements at Serpukov (Primakov) and Mainz (virtual pion) agree that the value for  $\alpha_\pi - \beta_\pi$  is approximately twice the size predicted by ChPT, albeit with large errors. The Compton scattering data are also in agreement with the dispersion calculation by Fil'kov.

Turning now to the  $\gamma\gamma \rightarrow \pi^+\pi^-$  data, the analysis by Babusci [Ba92] was limited by data sets with low statistics (MARK-II) and large systematic errors (see comments by Pennington in [Mo87]). It was also limited by the theoretical model, which was only one-loop in ChPT. Since then, considerable theoretical progress has been made in calculating  $\gamma\gamma \rightarrow \pi\pi$  cross sections; (i) Gasser *et al.* [Ga06] performed a two-loop calculation in ChPT, (ii) Donoghue and Holstein [Do93] established a connection between dispersion theory and ChPT by matching the low-energy chiral amplitude with the dispersion treatment, and (iii) Pasquini *et al.* [Pa08] performed a purely dispersive treatment for the cross section.

Fig. 2 shows predicted total cross sections from Pasquini *et al.* for  $\gamma\gamma \rightarrow \pi^+\pi^-$  for  $|\cos\theta_{\pi\pi}| < 0.6$ . The red curve is the Born approximation calculation with no polarizability effect. The black solid curve is an unsubtracted dispersion relation (DR) calculation with  $\alpha_\pi - \beta_\pi = 5.7$ , and the dashed curve is the subtracted DR calculation with the same polarizability. The dotted curve is the subtracted DR calculation with the polarizabilities from [Fi06] with  $\alpha_\pi - \beta_\pi = 13.0$ . Comparison of the subtracted DR curves with  $\alpha_\pi - \beta_\pi$  equal to 5.7 (dashed) and 13.0 (dotted), shows a change in the cross section at  $W_{\pi\pi} = 0.4$  GeV of approximately 20 percent. Therefore, a 4% statistical and systematic error in  $\sigma(\gamma\gamma \rightarrow \pi\pi)$  gives a 20% uncertainty in  $\alpha - \beta$ .

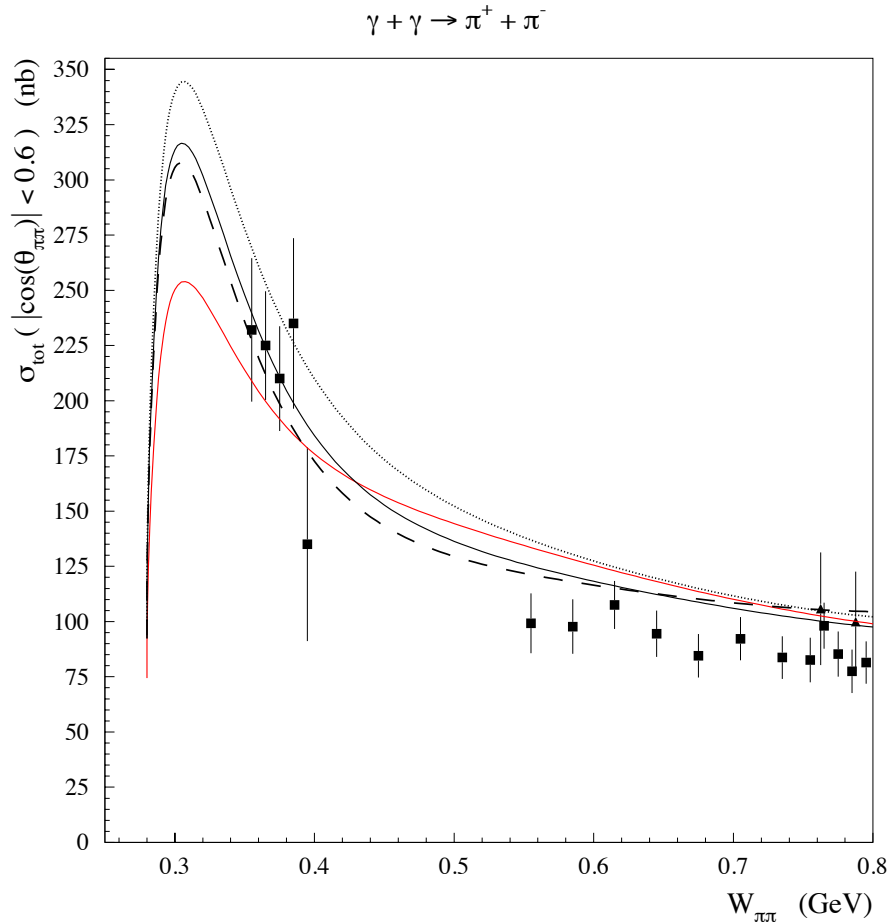


Figure 2:  $\gamma\gamma \rightarrow \pi^+\pi^-$  cross sections. Red curve: Born approx. (no polarizability effect); black solid: unsubtracted DR calculation with  $\alpha_\pi - \beta_\pi = 5.7$ ; dashed: subtracted DR with  $\alpha_\pi - \beta_\pi = 5.7$ ; dotted: subtracted DR with  $\alpha_\pi - \beta_\pi = 13.0$ . Data points are from MARK-II

The experimental data in the figure are from MARK-II [Bo92], where there are probably less than 200 events in the region of interest,  $W_{\pi\pi} < 0.5$  GeV. The figure clearly shows that the MARK-II data do not have the statistical precision, nor the coverage in  $W_{\pi\pi}$ , to provide a useful constraint on  $\alpha_\pi - \beta_\pi$ . Quoting Donoghue and Holstein [Do93], “*We conclude that although  $\gamma\gamma \rightarrow \pi^+\pi^-$  measurements certainly have the potential to provide a precise value for the pion polarizability, the statistical uncertainty of the present values does not allow a particularly precise evaluation.*”

## 4 Planned Future Measurements of the Pion Polarizability

There are two efforts underway to remeasure the charged pion polarizability: (1) COMPASS using the hadronic Primakoff effect with an incident pion beam, where they look for an exclusive  $\gamma\pi$  final state at very low  $t$ ; (2) measurements of  $\gamma\gamma \rightarrow \pi\pi$  at energies near threshold at Frascati.

COMPASS uses a 190 GeV pion beam on nuclear (Ni, W) targets. Pion Compton scattering is analyzed using the low energy expansion (LEX): at leading order in  $\omega$  the amplitude depends on the combination  $\alpha + \beta$  at forward angles, the combination  $\alpha - \beta$  at backward angles, and on unknown quadrupole polarizabilities at higher order in  $\omega$ . A dispersive calculation for pion Compton scattering, valid to all orders in  $\omega$ , does not exist. In the COMPASS analysis the measured  $E_\gamma/E_{beam}$  distribution is fit using a model for pion radiative production based on LEX with the constraint  $\alpha + \beta = 0$ , and the fit gives  $\alpha - \beta$ . Based on conference presentations, it is unclear what the photon-pion invariant mass resolution is, nor the resolution in  $\theta_{cm}$ . Several years ago COMPASS released a preliminary result for  $\alpha - \beta$  that was in agreement with ChPT, and then retracted the result. They have since taken more data and redone the analysis, and have presented a preliminary result in conferences that is in agreement with ChPT,  $\alpha - \beta = 3.8 \pm 1.4_{stat} \pm 1.6_{sys} \times 10^{-4}$ , where they constrain  $\alpha = -\beta$ . [Fr13]

Collider experiments, Frascati, have an advantage in that there is no nuclear background. However, it is difficult to reach low  $M_{\pi\pi}$  because low energy pions will stop, decay in flight, or undergo multiple scattering before reaching the detector. The  $\mu^+\mu^-$  backgrounds are large in these experiments, approximately 5 times larger than the  $\pi^+\pi^-$  signal, complicating the measurement even further. The principle PID tool that MARK II utilized in their analysis was TOF; calorimeter measurements were less decisive because of the low pion energies [Bo92]. TOF will not be useful for the JLab measurement because of the extreme relativistic velocities of the pions, and the plan is to use a system of hadronic absorbers with MWPC's to distinguish pions from muon. The JLab experiment will utilize linearly polarized incident photons, and the  $(1 - \cos 2\phi_{\mu\mu})$  azimuthal dependence of the  $\mu\mu$  system can be used to help identify

muon backgrounds.

## 5 Measurements of the charged pion polarizability at Jefferson Lab Hall D

We propose to make measurements of  $\gamma\gamma \rightarrow \pi^+\pi^-$  cross sections via the Primakoff effect using the GlueX detector in Hall D. The differential cross section for Primakoff two-pion photoproduction with linearly polarized photons is given by [Ha66], [St71], [Bu75]

$$\frac{d^2\sigma}{d\Omega_{\pi\pi}dW_{\pi\pi}} = \frac{2\alpha Z^2 E_\gamma^4 \beta^2 \sin^2 \theta_{\pi\pi}}{\pi^2 W_{\pi\pi} Q^4} |F(Q^2)|^2 \sigma(\gamma\gamma \rightarrow \pi\pi) (1 + P_\gamma \cos 2\phi_{\pi\pi}) \quad (8)$$

In these expressions,  $\Omega_{\pi\pi}$  is the solid angle in the laboratory frame for the emission of the  $\pi\pi$  system,  $W_{\pi\pi}$  is the  $\pi\pi$  invariant mass,  $Z$  is the atomic number of the target,  $\beta$  is the velocity of the  $\pi\pi$  system,  $E_\gamma$  is the energy of the incident photon,  $F(Q)$  is the electromagnetic form factor for the target with final-state-interaction (FSI) corrections applied,  $\theta_{\pi\pi}$  is the lab angle for the  $\pi\pi$  system,  $\phi_{\pi\pi}$  is the azimuthal angle of the  $\pi\pi$  system relative to the incident photon polarization, and  $P_\gamma$  is the incident photon polarization.

### 5.1 Experimental conditions

This experiment uses the photon beamline and detector in Hall D to perform a measurement of the pion polarizability. Most of the experimental equipment is in place, but a few changes from the nominal conditions and additions to the experimental equipment will be necessary. The differences between our configuration and the nominal Hall D configuration are summarized in Table 1.

We propose to take advantage of the linear polarization of the photon beam, but set the position of the coherent peak between 5.5 and 6 GeV. The experimental target will be placed upstream of the nominal GlueX target by 64 cm ( $z=1$  cm in the Hall D coordinate system). This will improve the acceptance of small-angle pairs. Finally, we will add a detector to identify muons at small angles behind FCAL with two objectives - to separate the muon background efficiently, and to collect a clean sample of muon pairs for the experiment normalization.

Table 1: Configuration of the charged pion polarizability experiment compared to nominal GlueX. Detectors not identified in the table are assumed to be operated under the same conditions as in the nominal configuration.

Configuration	Nominal GlueX	This Experiment
Electron beam energy	12 GeV	12 GeV
Electron current	220 nA	50 nA on 20 $\mu\text{m}$ diamond
Coherent peak	8.4 – 9.0 GeV	5.5 – 6.0 GeV
Collimator aperture	3.5 mm	3.5 mm
Peak polarization	44%	76%
Coherent/Incoherent ratio	0.068	0.32
Tagging ratio	0.56	0.69
Target position	65 cm	1 cm
Target, length	H, 30 cm	$^{116}\text{Sn}$ , 0.060 cm
Start counter	nominal	removed
Muon identification	None	Behind FCAL

## 5.2 Photon beam

Taking data with the coherent peak set at 5.5–6.0 GeV (called 6 GeV for short) instead of the nominal configuration for GlueX improves the conditions for this experiment by a significant margin. This configuration improves the figure-of-merit (FOM) for the experiment by increasing the average polarization, increasing the coherent signal relative to the incoherent background, and improving the tagging ratio (see Figs. 3–8). The maximum linear polarization ( $P$ ) in the peak increases from 44% to 76%, the coherent signal increased by a factor of 4.7 relative to the incoherent background ( $S/B$ ) and the tagging efficiency ( $\epsilon_{tag}$ ) from 0.56 up to 0.69. Constructing a FOM as follows

$$FOM = P^2 \times S/B \times \epsilon_{tag}, \quad (9)$$

the figure-of-merit is a factor of 17 larger with the coherent peak at 6 GeV compared to 9 GeV. This results in a considerable improvement in the quality of the experiment and drives the request for taking data at this lower energy setting. Because this experiment can be normalized using the accurately known production of muon pairs, we use the same 3.5 mm collimator as for the nominal GlueX running to enhance the polarization and increase the figure of merit.

Measurement of the coherent peak using the tagger microscope requires moving this detector from its nominal location downstream in order to cover the region for the new coherent peak at 6 GeV. The design of the tagging spectrometer allows for this change,

although the modification requires a couple of days for the change in configuration and some beam time to ensure proper alignment of the fiber detectors to the electron beam angle, as this angle changes considerably along the focal plane.

### 5.3 Target and Production rates

The choice of target for this measurement depends on several factors. Although the cross section for Primakoff reactions varies with  $Z^2$ , see Eqn. 8,  $Z^2 \times \text{atoms/cm}^2$  per unit radiation length is nearly independent of  $Z$  from uranium down to iron, with about a 20% drop from lead to iron. When the Primakoff equation 8 is integrated with realistic nuclear form factors, the curve of event rate per unit radiation length flattens out even more, because the form factor suppresses the cross section for heavy nuclei relative to light nuclei. Therefore, effectively there is little difference in rate between calcium and lead for a fixed radiation length target. The experimental acceptances are also nearly identical. In section 5.5 it is argued that when using lepton pair production as a normalizing reaction, the parameter  $Z\alpha$  should be minimized. If rate considerations were all that mattered, then  $^{40}\text{Ca}$  would be an acceptable target.

However, there are effects which tend to negate the advantages of low  $Z$ . One effect is the total hadronic rate for a fixed radiation length target, which increases as you go to lower  $Z$ . The second effect is the background from  $\rho^0$  relative to Primakoff production, which also increases with decreasing  $Z$ .

We are still considering target options, however we consider  $^{116}\text{Sn}$  as a good target choice. Tin has decreased  $Z\alpha$  relative to lead, .37 versus .60, and comparable total hadronic rates and  $\rho^0$  production rates. All of the acceptance calculations in this proposal were performed for lead, however the acceptances and rates for lead and tin are nearly identical.

Assuming a 5% radiation length tin target, and tagged 5.5 GeV photons at a rate of  $10^7$  photons/s, then the event rate for  $\pi^+\pi^-$  Primakov events integrated from threshold up to  $W_{\pi\pi}=500$  MeV is approximately 400 events/hour.

### 5.4 $\pi^+\pi^-$ Backgrounds

The largest  $\pi^+\pi^-$  background is from coherent  $\rho^0$  photo-production on the nuclear target. In the helicity frame (described in Fig. 9) the angular distribution of the pion pair is given by [Ba72]

$$\frac{dW}{d\cos\theta d\phi} = \frac{3}{8\pi} \sin^2\theta_\pi (1 + P_\gamma \cos 2\psi) \quad (10)$$

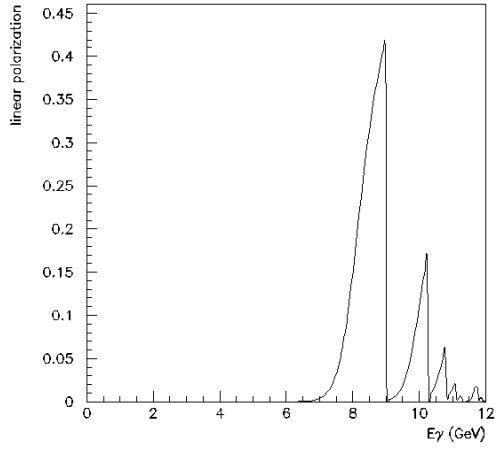


Figure 3: Polarization with peak at 9 GeV. The peak polarization is 44%.

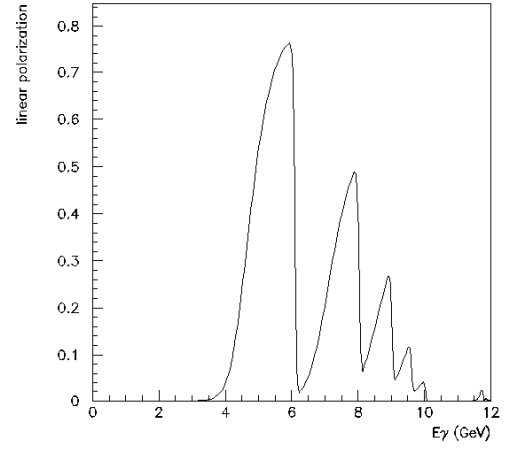


Figure 4: Polarization with peak at 6 GeV. The peak polarization is 76%.

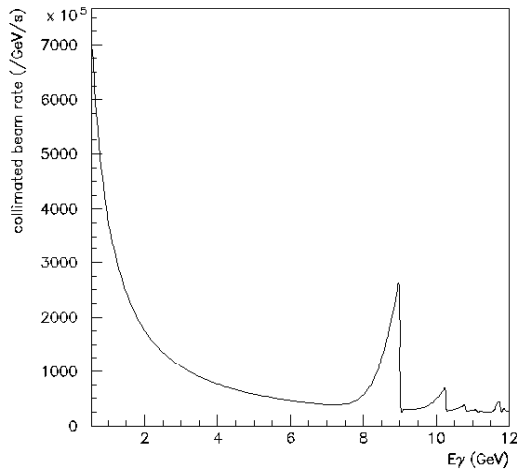


Figure 5: Collimated beam rate at 9 GeV. The ratio of events in the peak (8–9 GeV) to events outside the peak is 0.068.

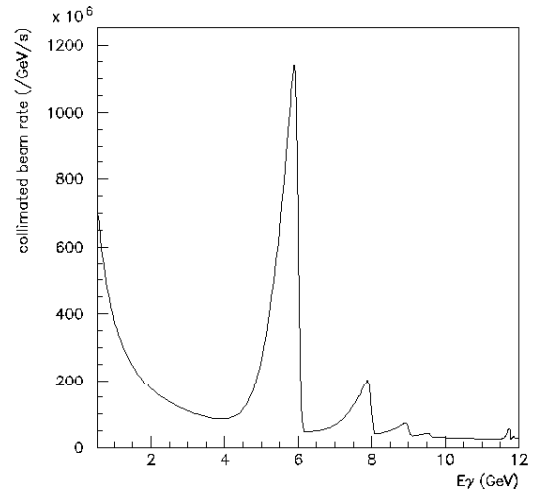


Figure 6: Collimated beam rate at 6 GeV. The ratio of events in the peak (5–6 GeV) to events outside the peak is 0.32.

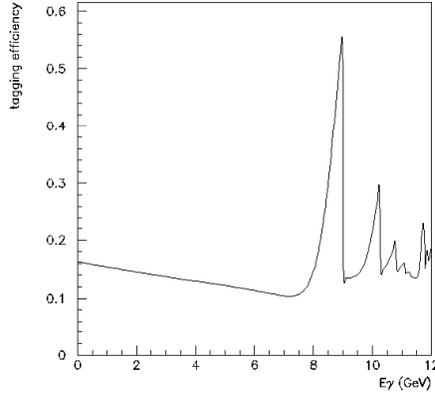


Figure 7: Tagging ratio with the peak at 9 GeV. The tagging ratio at the peak is 0.56.

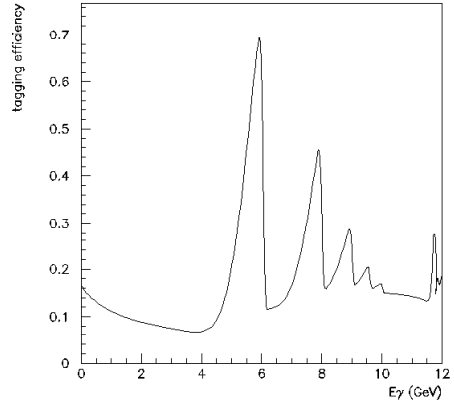


Figure 8: Tagging ratio with peak at 6 GeV. The tagging efficiency at the peak is 0.69.

where  $\psi$  is the azimuthal angle between the pion decay plane in the helicity frame and the polarization plane of the incident photon, and  $\theta_\pi$  is the polar angle in the same frame of the outgoing  $\pi^+$ . The differential cross section for  $\rho^0$  photo-production on nuclear targets is given by

$$\frac{d\sigma}{dt} = \sigma(0)e^{-At} \quad (11)$$

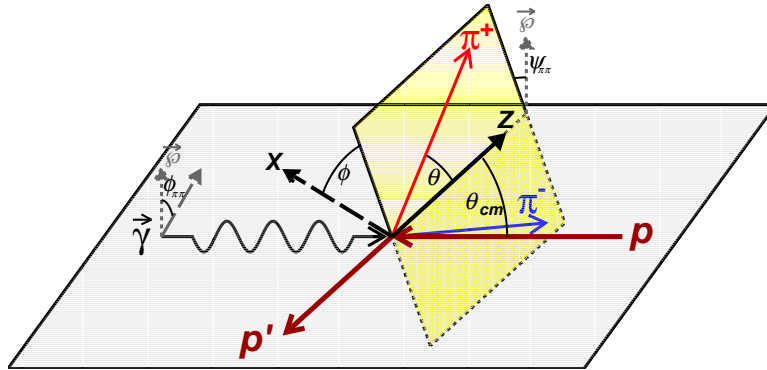


Figure 9: Diagram of the helicity frame for two pion photo-production on the nucleon

Other backgrounds result from nuclear coherent and incoherent production of  $\pi^+\pi^-$ . It can be expected that the nuclear coherent production will be small compared to co-

herent  $\rho^0$  production because a medium to heavy nuclear target acts as a filter to remove nuclear coherent events. This effect is clearly seen in the  $\pi^0$  angular distributions measured by the PrimEx experiment for carbon and lead [La11], and the effect will be even stronger for the  $\pi\pi$  final state. Because Primakoff production occurs approximately 100 fm from the nucleus, FSI has a relatively weak effect on the Primakoff process even for heavy nuclei [Mi11]. It is an open question as to how much strength there will be for  $0^+ \pi\pi$  production in the near threshold region from  $\gamma A \rightarrow f_0(600)A$ . We are planning to analyze  $\gamma p \rightarrow \pi^0\pi^0$  data from RadPhi to help constrain calculations of the nuclear coherent background [Jo13]. S. Gevorkyan will do the theoretical calculations for the coherent background, as well as the strong form factor used in the Primakoff equation.

Nuclear incoherent production can result from final state interactions of coherently produced  $\rho^0$  mesons with the nucleus. We are collaborating with T. Rodrigues, who did the nuclear incoherent calculations for PrimEx, on a similar calculation for this experiment [Ro].

Histograms of Primakoff and coherent  $\rho^0$  photo-production with the event weighting given by Eqns. 8, 10, and 11 are shown in Figs. 10, 11, 12, 13, 14, and 15. The  $W_{\pi\pi}$  distribution for  $\rho^0$  events is taken from a ZEUS analysis of high- $t$   $\rho^0$  photo-production on the proton [Br99]. The parameters  $\sigma(0)$  and  $A$  in Eqn. 11 are taken from references [Al70] and [As67], respectively.

Fig. 10 shows the  $2\pi$  invariant mass distribution for Primakoff and  $\rho^0$  events up to a cutoff at  $W_{\pi\pi} = 0.50$  GeV. The colors in the figure reference different regions in  $W_{\pi\pi}$ . In the blue region the Primakoff process dominates; in the red region  $\rho^0$  photo-production dominates; and in the green region the Primakoff and VMD strengths are approximately equal. Fig. 11 shows how the strength of the Primakoff process depends on  $W_{\pi\pi}$ . The kinematic values shown in figures 12-15 illustrate their dependence on  $W_{\pi\pi}$  using this same color scheme.

Fig. 12 shows the  $t$  distribution of events. The blue curve (primarily Primakoff) shows the characteristic peaking of the Primakoff process at very low angles [Mi11]. The red curve (primarily  $\rho^0$ ) is much flatter at low  $t$ , as expected by Eqn. 11.

Fig. 13 shows the distribution of azimuthal angles of the  $\pi\pi$  system in the lab frame, where the angle  $\phi_{\pi\pi}$  is measured relative to the incident photon polarization direction. The blue curve (primarily Primakoff) shows a prominent  $(1 + \cos 2\phi_{\pi\pi})$  characteristic from Eqn. 8, and the red curve (primarily  $\rho^0$ ) is nearly flat.

Fig. 14 shows the distribution of  $\cos\theta_{\pi^+}$  in the helicity frame. The blue curve (primarily Primakoff) is nearly flat because the threshold Primakoff pions are in s-waves. The red curve (primarily  $\rho^0$ ) shows the  $\sin^2\theta_\pi$  peaking from Eqn. 10.

Fig. 15 shows the distribution of azimuthal angles of the  $\pi^+$  in the helicity frame,

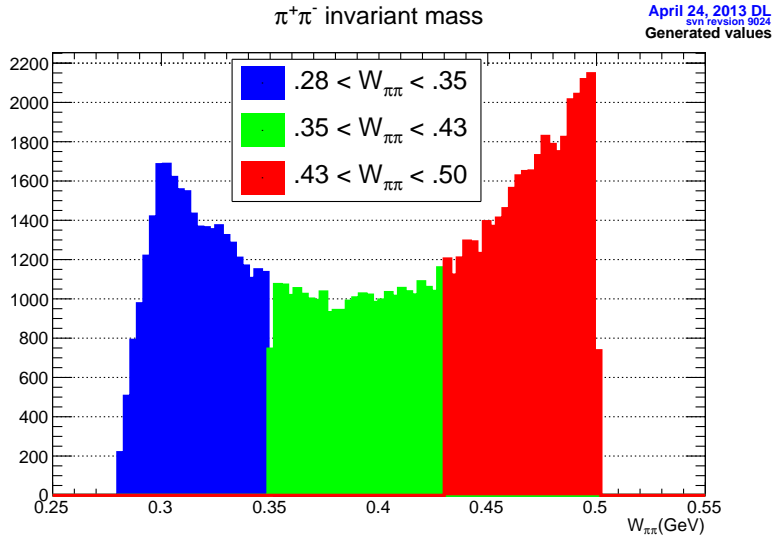


Figure 10: Histogram of  $W_{\pi\pi}$  for Primakoff and  $\rho^0$  events

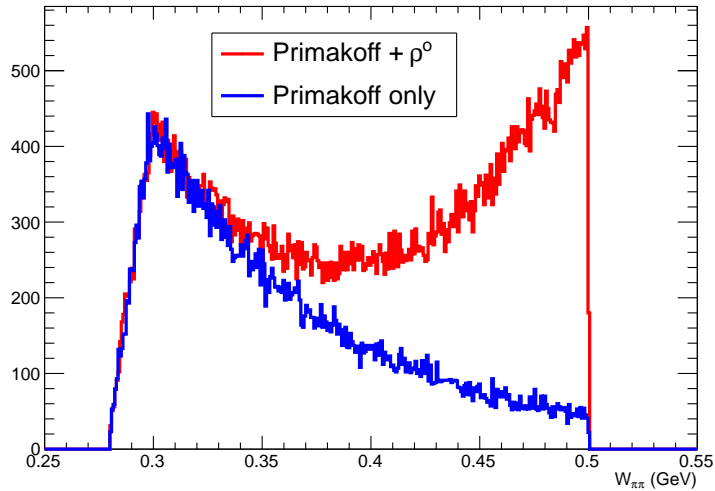


Figure 11: Histogram of  $W_{\pi\pi}$  for Primakoff (blue curve) and Primakoff +  $\rho^0$  events (red curve) events

where the angle  $\psi$  is measured relative to the incident photon polarization direction. The blue curve (primarily Primakoff) is nearly flat. The red curve (primarily  $\rho^0$ ) shows a prominent  $(1 + \cos 2\psi)$  characteristic from Eqn. 10.

To summarize, by utilizing the sensitivity demonstrated in the above figures to

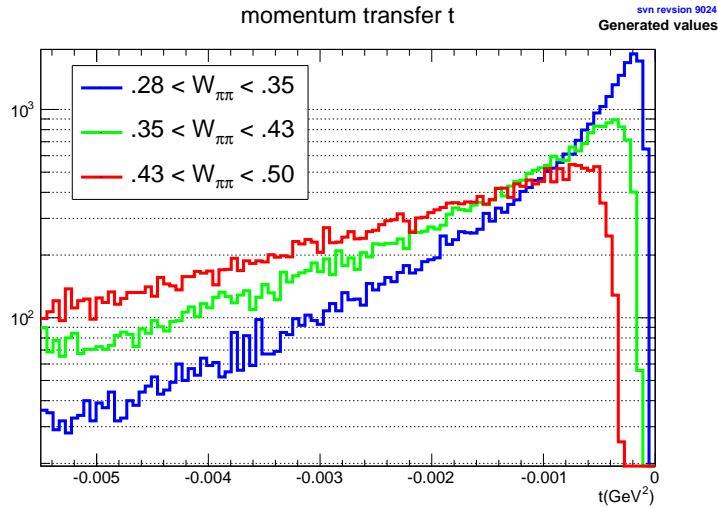


Figure 12: Histogram of  $t$  for Primakoff and  $\rho^0$  events. The blue curve is for events with  $0.28 < W_{\pi\pi} < 0.35$  GeV, green is for events with  $0.35 < W_{\pi\pi} < 0.43$  GeV, and red is for events with  $0.43 < W_{\pi\pi} < 0.50$  GeV.

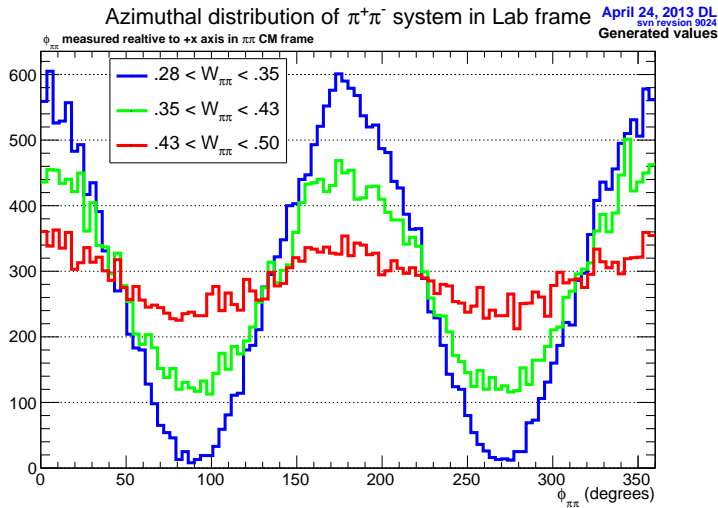


Figure 13: Histogram of  $\phi_{\pi\pi}$  for Primakoff and  $\rho^0$  events. The blue curve is for events with  $0.28 < W_{\pi\pi} < 0.35$  GeV, green is for events with  $0.35 < W_{\pi\pi} < 0.43$  GeV, and red is for events with  $0.43 < W_{\pi\pi} < 0.50$  GeV.

the incident linearly polarized photons, we can separate Primakoff contributions from coherent  $\rho^0$  photo-production by measuring (i) the azimuthal distribution of the  $\pi\pi$  system in the lab frame relative to the photon polarization, and (ii) the azimuthal

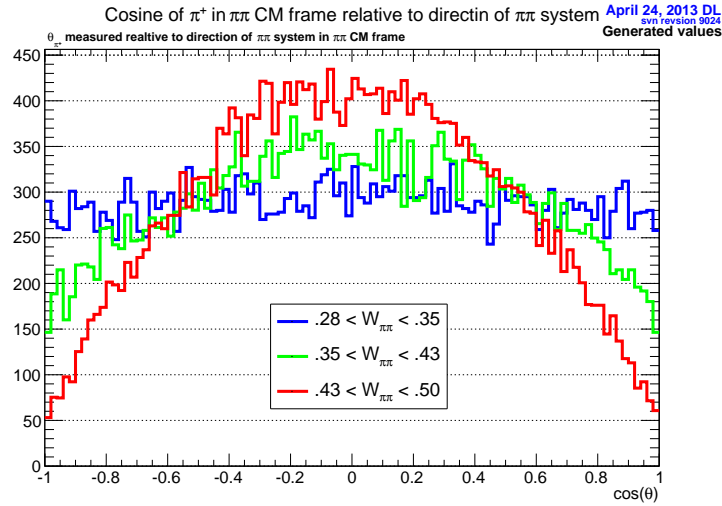


Figure 14: Histogram of  $\cos\theta_{\pi^+}$  in the helicity frame for Primakoff and  $\rho^0$  events. The blue curve is for events with  $0.28 < W_{\pi\pi} < 0.35$  GeV, green is for events with  $0.35 < W_{\pi\pi} < 0.43$  GeV, and red is for events with  $0.43 < W_{\pi\pi} < 0.50$  GeV

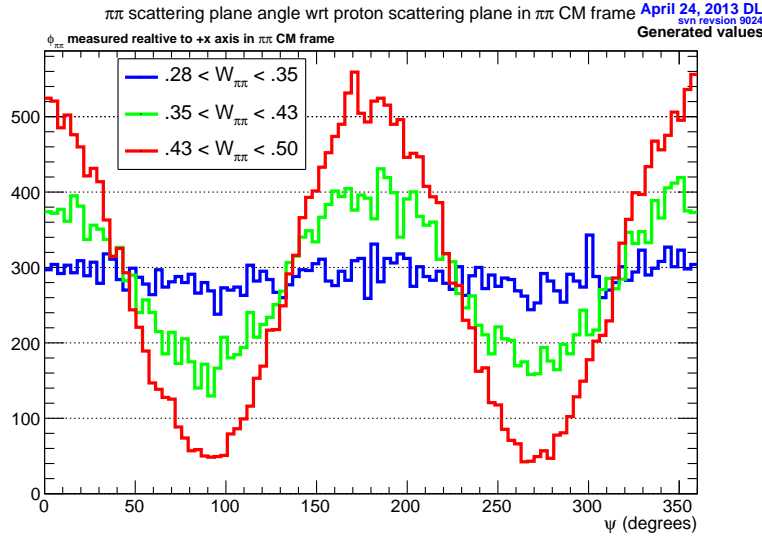


Figure 15: Histogram of  $\psi$  for Primakoff and  $\rho^0$  events. The blue curve is for events with  $0.28 < W_{\pi\pi} < 0.35$  GeV (primarily Primakoff), green is for events with  $0.35 < W_{\pi\pi} < 0.43$  GeV, and red is for events with  $0.43 < W_{\pi\pi} < 0.50$  GeV (primarily  $\rho^0$ ).

distribution of the  $\pi^+$  in the helicity frame relative to the photon polarization. The first criterion is exact, while the second criterion assumes helicity conservation in  $\rho^0$

photo-production.

## 5.5 Lepton Pair Backgrounds

To compare relative rates for  $\gamma A \rightarrow e^+e^-A$ ,  $\gamma A \rightarrow \mu^+\mu^-A$  and  $\gamma A \rightarrow \pi^+\pi^-A$ , it is convenient to calculate cross sections for  $\gamma\gamma \rightarrow e^+e^-$ ,  $\gamma\gamma \rightarrow \mu^+\mu^-$  and  $\gamma\gamma \rightarrow \pi^+\pi^-$ . The angular distributions are shown in Fig. 16, where the lepton pair cross sections are derived from expressions in Bjorken and Drell. The  $\pi^+\pi^-$  pair cross sections are from the MARK II data [Bo92]. The red, green and blue curves are for  $\mu^+\mu^-$ ,  $\pi^+\pi^-$  and  $e^+e^-$ , respectively, and the solid, dashed, and dash-dot curves are for CM energies of 300, 400, and 500 MeV. Over the angular range from 40 to 140 degrees, where GlueX has relatively good angular acceptance, the  $e^+e^-$  rate is negligible, and the muon:pion ratio can range from approximately 10:1 to 1:1. Because of the high muon rate relative to the pion rate, it will be necessary to instrument GlueX with a forward angle muon veto counter placed behind FCAL. Details of the detector system are given in Appendix A.

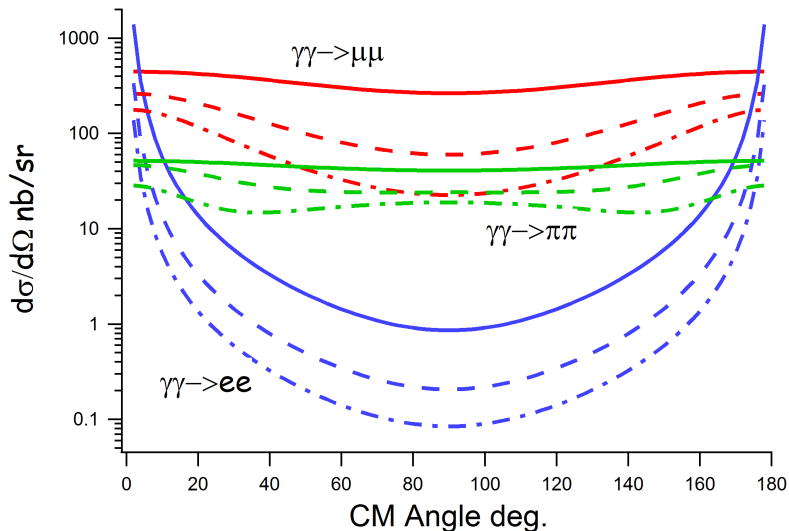


Figure 16: Angular distributions for  $e^+e^-$ ,  $\mu^+\mu^-$  and  $\pi^+\pi^-$  pairs are shown as red, green and blue curves, respectively. The solid, dashed, and dash-dot curves are for 300, 400 and 500 MeV CM energies.

Although the  $\mu^+\mu^-$  background does present a significant experimental challenge, it also provides a QED signal that  $\pi^+\pi^-$  yields can be normalized to. The issue then becomes how accurately theory can predict  $\mu^+\mu^-$  cross sections. The amplitudes for  $\gamma A \rightarrow e^+e^-A$  on carbon are listed below in order of decreasing importance: (i)

Bethe-Heitler pair production on the nucleus with atomic screening  $\approx 80$  % (ii) pair production on atomic electrons  $\approx 20$  % (iii) QED radiative corrections of order  $\alpha/\pi$  with respect to the dominant Bethe-Heitler term, 1-2 % (iv) nuclear incoherent production on protons, 0.05 % and (v) virtual Compton scattering,  $\gamma A \rightarrow \gamma^* A \rightarrow e^+ e^- A$ ,  $10^{-5}$  %. During the PrimEx experiment, pair production cross sections on carbon were measured with experimental errors of  $\pm 0.58$  (stat) %  $\pm 1.13$  (sys) % [Te08]. The theoretical calculation by Korchin [Ko08] is in good agreement with these results.

For coherent muon pair production, where both muons are detected, the most important amplitudes from the above list are (i), Bethe-Heitler pair production, (iv) nuclear incoherent production, and (v) virtual Compton. To calculate the Coulomb corrections accurately, it is important that  $Z\alpha$  should not be too large. For this reason we do not consider lead,  $Z\alpha = .58$ , as the best production target for this experiment. We are instead considering a medium weight nucleus,  $^{116}\text{Sn}$  with  $Z\alpha = 0.36$ . We plan to enlist Korchin in calculating the muon cross sections.

The muon signal can also provide a measurement of the photon polarization. For linearly polarized photons the azimuthal distribution of the  $\mu^+ \mu^-$  system is given by [Ba08]

$$\frac{d\sigma}{d\Omega_{\mu\mu}} \propto |(\vec{\epsilon} \times \vec{q}) \cdot \vec{q}|^2 \propto \cos^2 \phi_{\mu\mu} \propto 1 - \cos 2\phi_{\mu\mu} \quad (12)$$

As discussed later in this proposal, another technique for measuring the photon polarization is through coherent  $\pi^0$  photo-production on a spin-zero target. The muon asymmetry can provide a technique complementary to the  $\pi^0$  method for extracting the photon polarization directly from the data.

## 5.6 Azimuthal separation of signal from background

Under some restrictive assumptions about the physics backgrounds in the experiment, it is possible to separate the the Primakoff  $\pi^+ \pi^-$  signal from  $\mu^+ \mu^-$  and  $\rho^0$  backgrounds by measuring azimuthal distributions relative to the incident photon polarization. Note that fitting the azimuthal distribution of the pion in the helicity frame fixes the contributions  $N_{\pi\pi} + N_{\mu\mu}$ , and  $N_\rho$  ( see Eqn. 10), while fitting the azimuthal distribution of the  $\pi\pi$  ( $\mu\mu$ ) system in the lab frame fixes  $N_{\pi+\pi} - N_{\mu\mu}$ , (see Eqns. 12 and 8 ). Then based on these two fits, it is possible to extract  $N_{\pi\pi}$ . The limitations of this technique are that it assumes the validity of helicity conservation in  $\rho^0$  photo-production, and that there are no other backgrounds present other than the  $\mu\mu$  and  $\rho^0$  backgrounds. The extent of helicity conservation in  $\rho^0$  photo-production can be measured in the data, and this uncertainty can be minimized. This is a promising technique that we can exploit to test analyses using the muon detection system.

## 5.7 Acceptance, Resolution, Trigger, and Rates

The standard GlueX simulation and reconstruction software *sim-recon* has been used to study the detector acceptance and resolution for the event topology in the kinematic regime of interest. The simulation is based on GEANT3 and has a detailed description of the geometry (Fig. 17 shows a diagram of the GlueX detector). Hits generated by the simulation are smeared using known detector resolutions. Full reconstruction is done using the smeared hits. This includes track finding and track fitting using a Kalman filter tracking program developed for GlueX. Some enhancements of the base GlueX software were made to accommodate the modified geometry of the current proposal. In particular, we used the kinematic fitting package in order to take advantage of our thin solid target's small extent in  $z$  as compared to the 30 cm  $LH_2$  target used by GlueX. Also, the Start Counter detector was removed from the geometry for simulations related to the current proposal.

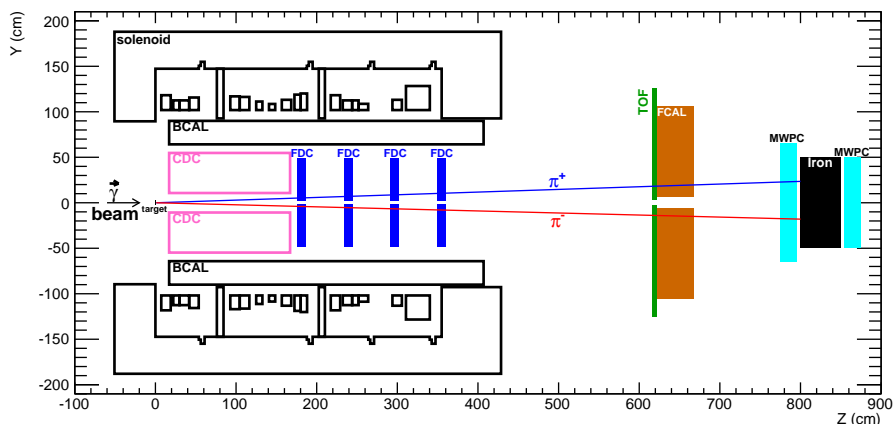


Figure 17: Diagram of the GlueX detector

A Monte Carlo study was performed to determine the acceptance of the detector for various  $z$ -locations of the solid target, in this case  $^{208}\text{Pb}$ . The kinematics of the reaction  $\gamma A \rightarrow A\pi^+\pi^-$  results in very forward going pions so acceptance can be gained by moving the target further upstream. This is because the FDC has a fixed sized dead region around the beam line. The GlueX design goal for the FDC was to reconstruct 1 GeV/c pions at  $\theta \geq 1^\circ$  coming from the center of the  $LH_2$  target at  $z=65$  cm in lab coordinates. Figure 18 shows two plots resulting from the study. They show a relatively modest gain in overall acceptance. However, Figure 19 shows the acceptance as a function of invariant mass  $W_{\pi\pi}$  for two target positions. This plot indicates that moving the target upstream shifts some of the acceptance to lower values of  $W_{\pi\pi}$ , the Primkoff region (see Fig. 11). Overall, the acceptance for  $\gamma Pb \rightarrow Pb\pi^+\pi^-$  events from

500 MeV down to threshold ( $=2m_\pi$ ) is about 50%.

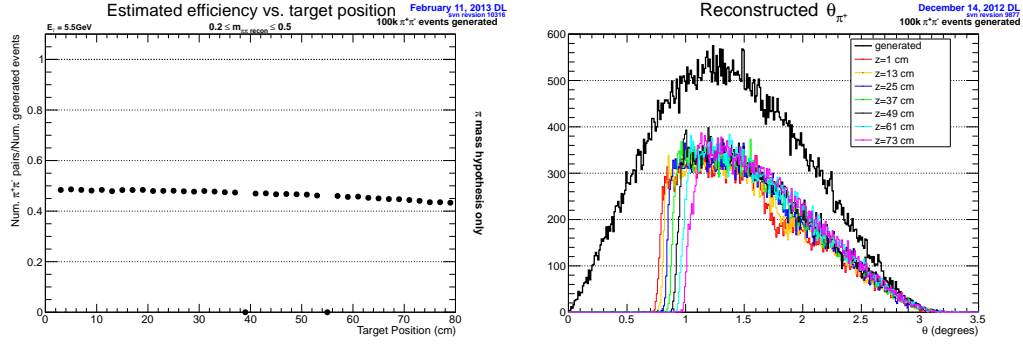


Figure 18:  $\pi^+\pi^-$  acceptance as a function of the target  $z$ -position. On the left is the acceptance vs. target  $z$ . On the right is the reconstructed  $\pi^+$   $\theta$  for several target positions in  $z$ .

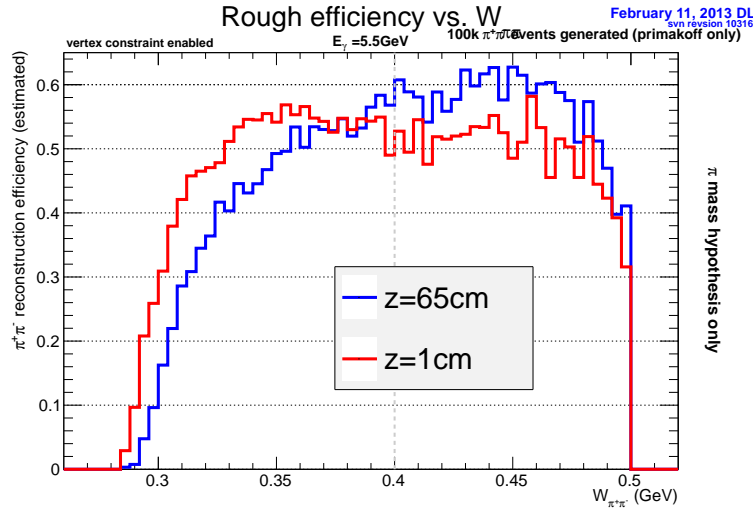


Figure 19: Acceptance of  $\pi^+\pi^-$  events for locating the Pb target at the nominal location of the center of the GlueX target ( $z=65$  cm) and the location being considered for the current measurement 64 cm upstream at  $z=1$ .

The angular resolutions of the individual reconstructed pion tracks can be seen in Figure 20. Resolutions of 40 mrad in  $\phi$  and 1 mrad in  $\theta$  are expected in the relevant region of phase space. Figure 21 shows the resolutions for the  $\pi^+\pi^-$  system. The resolution of  $\phi_{\pi\pi}$  is considerably worse ( $\sim 300$  mrad) than that of individual tracks due to transverse momentum resolution. Nonetheless, this is sufficient to resolve the  $1 + \cos 2\phi_{\pi\pi}$  dependence of events generated via the Primakoff shown in the lower left plot of the figure.

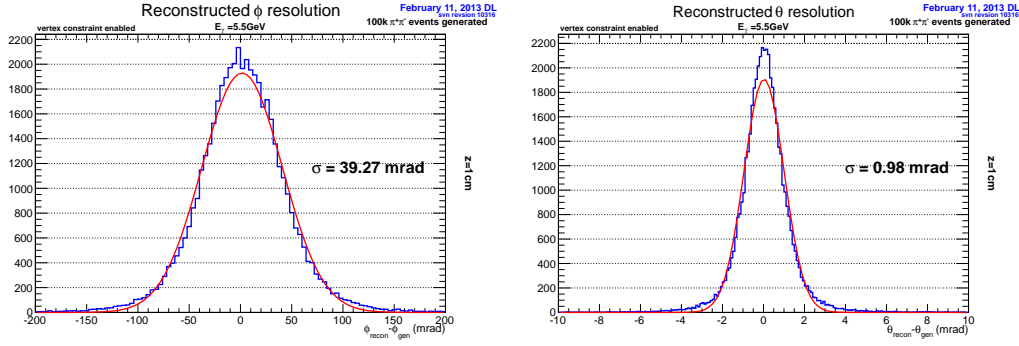


Figure 20: Reconstructed angular resolutions for single tracks. The red curves are from Gaussian fits to the blue distributions.

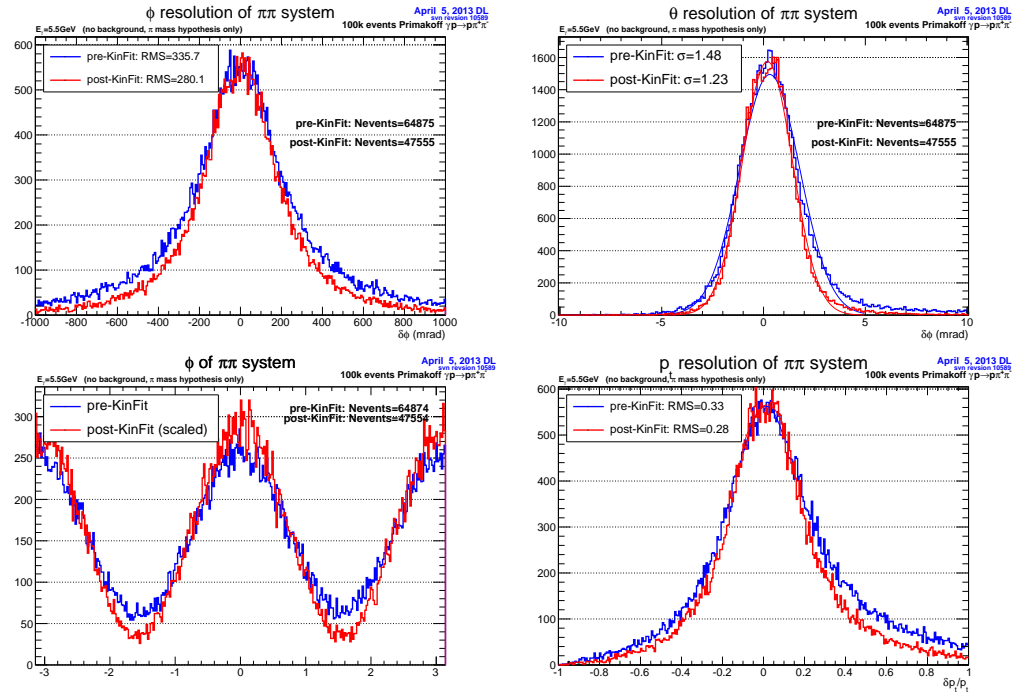


Figure 21: Reconstructed resolutions of kinematic variables  $\phi$ ,  $\theta$ , and  $p_t$  for the  $\pi\pi$  system. Blue represents before a kinematic fit is performed and red is after.

Figure 22 shows the resolution of the invariant mass  $W_{\pi\pi}$ . This shows that considerable improvement can be achieved by using a kinematic fitter to constrain the total 4-momentum to that of the incident beam photon. As shown in the plot, the kinematic fitter gives considerable improvement resulting in a resolution of about 4 MeV in  $W_{\pi\pi}$ . This is sufficient to sort the data into multiple bins in  $W_{\pi\pi}$  allowing the  $1 + P_\gamma \cos 2\phi_{\pi\pi}$

and  $1 + P_\gamma \cos 2\psi_{\pi\pi}$  dependence to be checked (see figures 13 and 15).

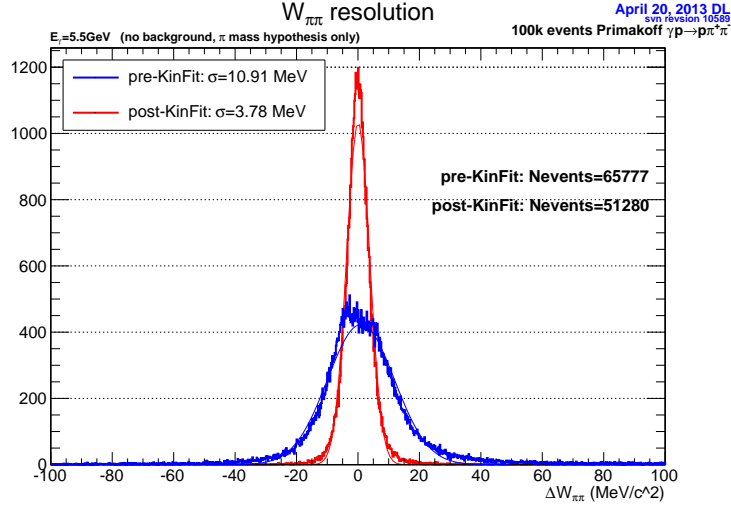


Figure 22: Reconstructed invariant mass  $W_{\pi^+\pi^-}$ . The blue is before a 4C kinematic fit is performed and the red is after.

### 5.7.1 Trigger and rates

Triggering for the current measurement will use the standard GlueX hardware, which will be configured to look for one or more clusters in the FCAL calorimeter above a certain threshold. The GlueX trigger consists of an open trigger designed to be efficient for all hadronic events above 4 GeV when the coherent peak is set between 8.4 and 9.0 GeV. The trigger will be formed primarily from a combination of sums from the BCAL and FCAL calorimeters [Somov1043]. Digitized sums will be presented to the FPGA trigger logic every 4 ns, allowing triggers to be formed from total energy deposition in the calorimeter. For the GlueX configuration, the hadronic rate for  $10^7 \gamma/s$  in the coherent peak is 35 kHz, which is reduced by the Level 1 trigger to less than 20 kHz for an energy threshold in the FCAL of 500 MeV when no energy is deposited in the BCAL. Approximately half of the triggers are hadronic events and half are due to electromagnetic pileup. This results in a 93% efficiency for triggering on three charged pions.

For this experiment, the total hadronic rate for a  $10^7 \gamma/s$  of collimated flux between 5.5 and 6 GeV incident on a 5 % radiation length Sn target is less than 3.5 kHz, well below the DAQ limit of 20 kHz. The trigger condition will also be open and the selection of the two pion signal will be accomplished during offline reconstruction. The FCAL will be used for triggering on the pion pair, but in order to be efficient for

our two-pion trigger, the thresholds in the FCAL will need to be reduced below 100 MeV. Figure 23 shows the distribution of hadronic events surviving a single 30 MeV threshold cut in the FCAL, which eliminates the events produced by photons with energies of less than about 3 GeV, well below the coherent peak. However, most of the trigger rate for low thresholds in the FCAL is due to the electromagnetic backgrounds, which contribute 10 kHz at a threshold of 100 MeV. In order to reduce the threshold in the FCAL even further, we will need to select coincident hits in the time-of-flight scintillators and veto on energy in the BCAL.

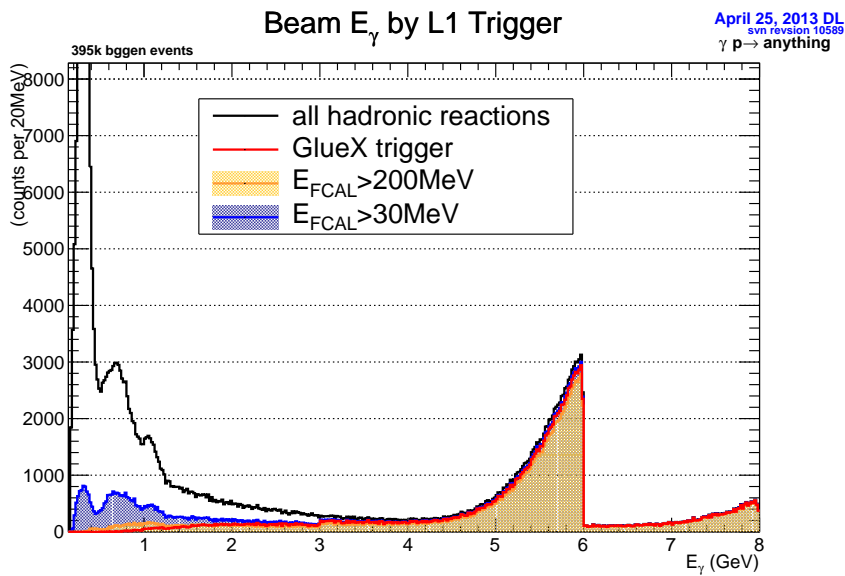


Figure 23: Level-1 trigger selection of incident photon energies. The  $E_{FCAL} > 30\text{MeV}$  trigger accepts about 45% of all hadronic interaction events with a bias towards higher energies.

## 5.8 $\pi^0$ Primakoff Normalization

The Primakoff  $\pi^0$  photoproduction will be used to monitor the degree of linear polarization of the incident photon beam. For a linearly polarized beam with polarization  $P_\gamma$ , the differential cross section at a given photon energy is

$$\frac{d\sigma_{pol}}{d\Omega}(\theta, \varphi) = \frac{d\sigma}{d\Omega}(\theta)[1 - P_\gamma \Sigma(\theta) \cos 2(\varphi - \varphi_\gamma)] \quad (13)$$

where  $d\sigma/d\Omega$  is the unpolarized differential cross section,  $\Sigma(\theta)$  is the beam asymmetry,  $\varphi$  is the azimuthal angle of the reaction plane and  $\varphi_\gamma$  is the direction of the photon polarization vector. Performing measurements with vertical ( $\varphi_\gamma = \pi/2$ ) and horizontal ( $\varphi_\gamma = 0$ ) polarizations, one can obtain the azimuthal yields normalized by flux,  $N_v(\varphi)$

and  $N_h(\varphi)$ , for vertical and horizontal polarizations, respectively. Assuming that detection efficiency and  $P_\gamma$  do not depend on the polarization state and knowing that the beam asymmetry  $\Sigma = 1$  for the Primakoff  $\pi^0$  photoproduction, one can write

$$\frac{N_v(\varphi) - N_h(\varphi)}{N_v(\varphi) + N_h(\varphi)} = P_\gamma \cos 2\varphi \quad (14)$$

Fitting the measured ratio in the left part of Eqn. 14 to the function  $P_\gamma \cos 2\varphi$ , it is possible to extract the value of  $P_\gamma$ .

To check the possibility of such a measurement, 100k events with  $\pi^0$  produced in the Pb target by horizontally and vertically polarized photons with  $P_\gamma = 1$  were simulated. The energy of the  $\pi^0$  was 5.5 GeV. Fig. 24 shows the generated  $\theta_{\pi^0}$  and  $\varphi_{\pi^0}$  distributions which correspond to the Primakoff mechanism of  $\pi^0$  photo-production.

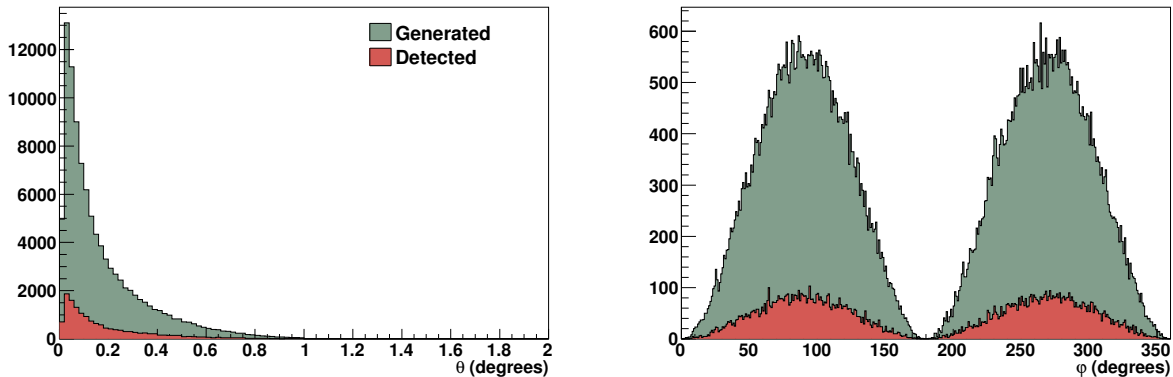


Figure 24: Distribution of  $\theta_{\pi^0}$  and  $\varphi_{\pi^0}$  for generated and accepted events.

Identification of the  $\pi^0$  events was done via reconstruction of the  $2\gamma$  invariant mass of  $\pi^0$  decay. Accepted and rejected events are shown in Fig. 25. The ratio between the accepted and generated  $\pi^0$  events is plotted in Fig. 26 as a function of  $\theta_{\pi^0}$ .

The procedure of extracting  $P_\gamma$  is shown in Fig. 27. The reconstructed ratio  $\frac{N_v(\varphi) - N_h(\varphi)}{N_v(\varphi) + N_h(\varphi)}$  is fitted by  $P_\gamma \cos 2\varphi$  leaving  $P_\gamma$  free. One can see that the generated 100k+100k events with  $\approx 15\%$  acceptance of  $\pi^0$  allows us to extract the photon polarization degree  $P_\gamma$  with about 1% precision.

The data selection criteria for coherent  $\pi^0$  photo-production are discussed in references [La11] and [Mi11]. In this case we select nuclear coherent events, not the Primakoff events, because the nuclear coherent events are emitted at larger angles, where the detector has better  $\phi$  resolution.

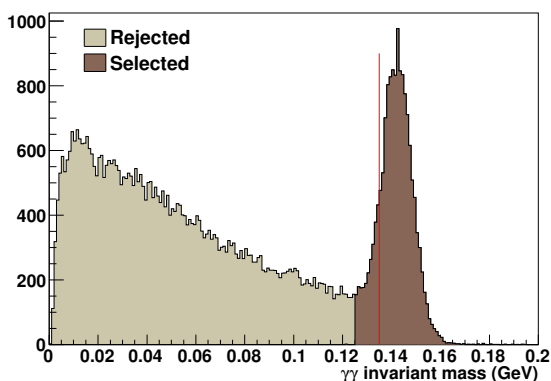


Figure 25:  $2\gamma$  invariant mass. Selected events are painted dark-brown. The red line indicates the  $\pi^0$  mass.

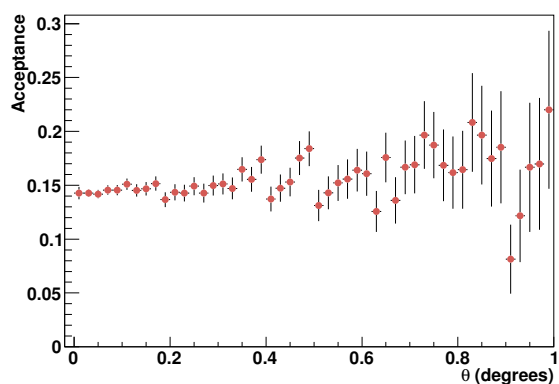


Figure 26: Ratio of the accepted (detected) to generated  $\pi^0$  events.

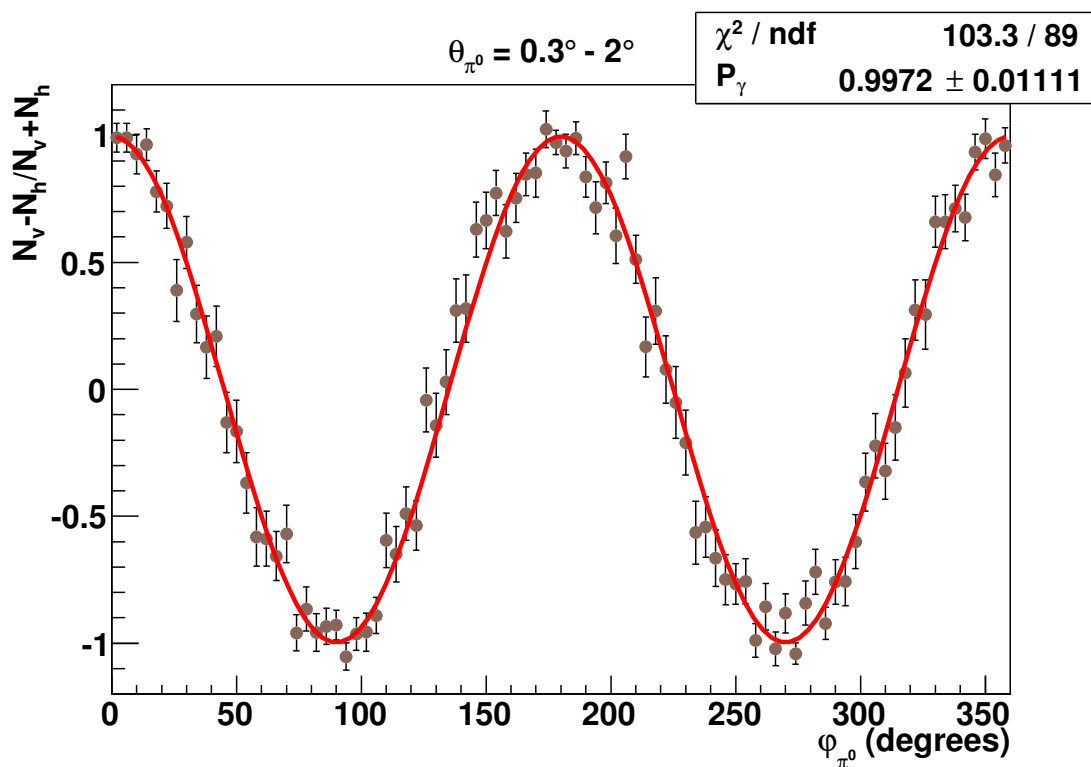


Figure 27: The function  $P_\gamma \cos 2\varphi$  fitted to the ratio  $\frac{N_v(\varphi) - N_h(\varphi)}{N_v(\varphi) + N_h(\varphi)}$  with  $P_\gamma$  as the free parameter.

Table 2: Statistical errors, correction factors, and uncertainties in correction factors.

Errors and correction factors	Correction factor	Statistical uncertainty in correction factor
Overall statistical error		0.6 %
Normalization to $\mu^+\mu^-$ and relative trigger efficiency		1 %
$\mu^+\mu^-$ background in $\pi^+\pi^-$ yield	0.03 %	0 %
Polarization	70%	0.2 %
Pion identified as muon, and pion decay	8 %	1%
Total systematic error		1.5 %
Projected error in $\alpha - \beta$		10%

## 5.9 Errors and Sensitivity

The anticipated statistical errors, including the error from azimuthal fitting of the data, are shown in Fig. 30. The errors assume 20 days of running on a 5 % radiation length  $^{116}\text{Sn}$  target,  $10^7$  photons/s, and nominal acceptance for  $\pi^+\pi^-$ . Table 2 summarizes the estimated statistical and systematic errors. In the following we describe each of these contributions in detail:

- Overall statistical error: This aggregate error is based on fitting the  $\phi_{\pi\pi}$  distribution to extract the Primakoff yield, and then fitting a theoretical curve to the  $W_{\pi\pi}$  data points (see figures 28-30).
- Normalization to  $\mu^+\mu^-$  and relative trigger efficiency: This is the estimated uncertainty for a calculation of  $\gamma A \rightarrow \mu^+\mu^- A$  of uncertainties in the relative trigger efficiencies of pions versus muons, 1 %.
- $\mu + \mu^-$  background in  $\pi^+\pi^-$  yield: The background considered here is the case where a muon fails to trigger the muon detector behind the iron shield. If we assume the muon chamber has x, u, v planes with 95% plane efficiency for minimum ionizing particles, then the overall chamber efficiency is 99.3%. Assuming a 5:1 muon:pion ratio, then the probability for both tracks failing to trigger the muon counter is very small, 0.03%. The efficiency of the muon counter can be measured by examining events in kinematics where muon pair production dominates, where one track tags as a muon, then measuring the probability for the second track to tag as a pion.
- Polarization: The photon polarization is determined by measuring the azimuthal distribution of (i)  $\mu^+\mu^-$  pairs, and (ii)  $\pi^0$  from coherent photo-production. Since

there are approximately five times as many  $\mu^+\mu^-$  pairs in the data as compared to  $\pi^+\pi^-$ , the statistical precision will be very high in this method, approximately 0.2 %. The purity of the  $\mu^+\mu^-$  sample will not be a limiting factor. Pion contamination can be estimated by assuming 5 hadronic interaction lengths for FCAL + iron absorber, then the probability for a pion to punch through is approximately 0.7 %. The probability for both pions to punch through, weighted by the 1:5 pion:muon ratio, is negligible. Pions can also register as muons through pion decay (see discussion below for “One or both pions decays in flight”). Taking the worst case that all 4 % of the pions that decay will be tagged as muons, gives a pion contamination in the muon yield of 0.03 %.

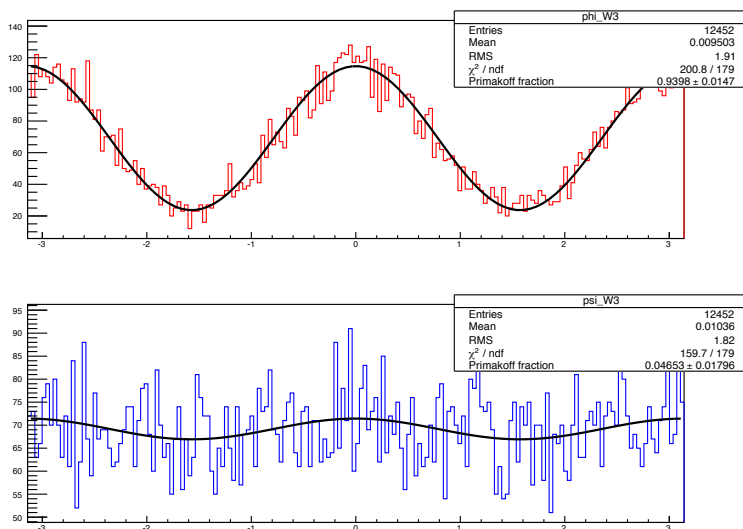


Figure 28: Example fits of the  $\phi_{\pi\pi}$  spectrum (top, red) and the  $\psi_{\pi\pi}$  spectrum (bottom, blue) for the  $W_{\pi\pi}$  bin centered at  $330\text{MeV}/c^2$ . The polarization was fixed at 70% (corresponding to the generated data set). The one free parameter of the fit gave either the fraction of Primakoff (top) or  $\rho^o$  (bottom) events. The angles used here are from generated values, but with a cut on  $\theta > 0.8^\circ$  to represent the acceptance of the detector.

- Pion identified as muon, and pion decay: These issues are linked, through pion decay, and require a unified calibration treatment using simulation and data analysis. To limit the uncertainty in correcting the data we expect that it will be necessary to carefully simulate pion decay in the experiment, and calibrate the simulation relative to experimental data. Calibration data might be taken in a kinematic regime where  $\gamma A \rightarrow \rho^0 A$  dominates over muon pair production by several orders of magnitude. We are developing a detailed simulation of the experimental setup to study the effects of pion decay. The overall correction factor for these effects will be approximately 8 %. We believe that by careful simulation,

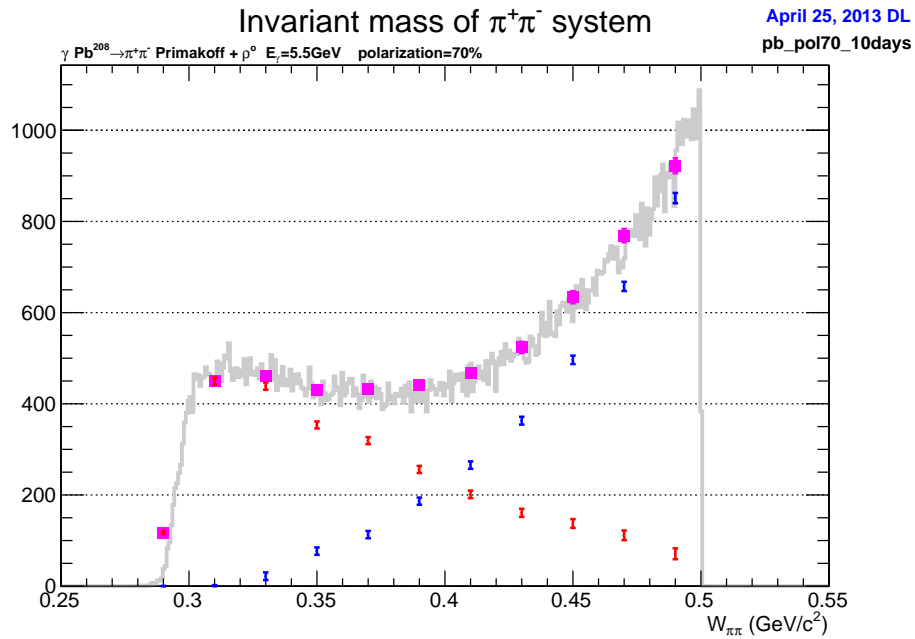


Figure 29: Results of all fits similar to those shown in Figure 28. The fractions obtained from the  $\phi_{\pi\pi}(\psi_{\pi\pi})$  dependent fits are used to calculate the number of Primakoff( $\rho^0$ ) events in each  $W_{\pi\pi}$  bin. The red(blue) markers indicate the extracted number of events of each type in the bin and the magenta squares are the sums of the red and blue points in each bin. Values used here are generated, but with a cut on  $\theta > 0.8^\circ$  to represent the acceptance of the detector.

and calibration of the simulation to experimental data, the uncertainty in this correction factor can be limited to  $\approx 1\%$ .

- Total systematic error: Combining the systematic errors in quadrature gives 1.5%.
- Projected error in  $\alpha - \beta$ : Combining the statistical and systematic errors in quadrature, and using the approximate sensitivity of the cross sections to  $\alpha - \beta$ , ( $\Delta(\alpha - \beta)/\Delta\sigma = 130\%/20\%$ ), gives an estimated error of 10 %. The absolute error in  $\alpha - \beta$  is therefore  $\pm 0.6 \times 10^{-4} fm^3$ .

$$\gamma + \gamma \rightarrow \pi^+ + \pi^-$$

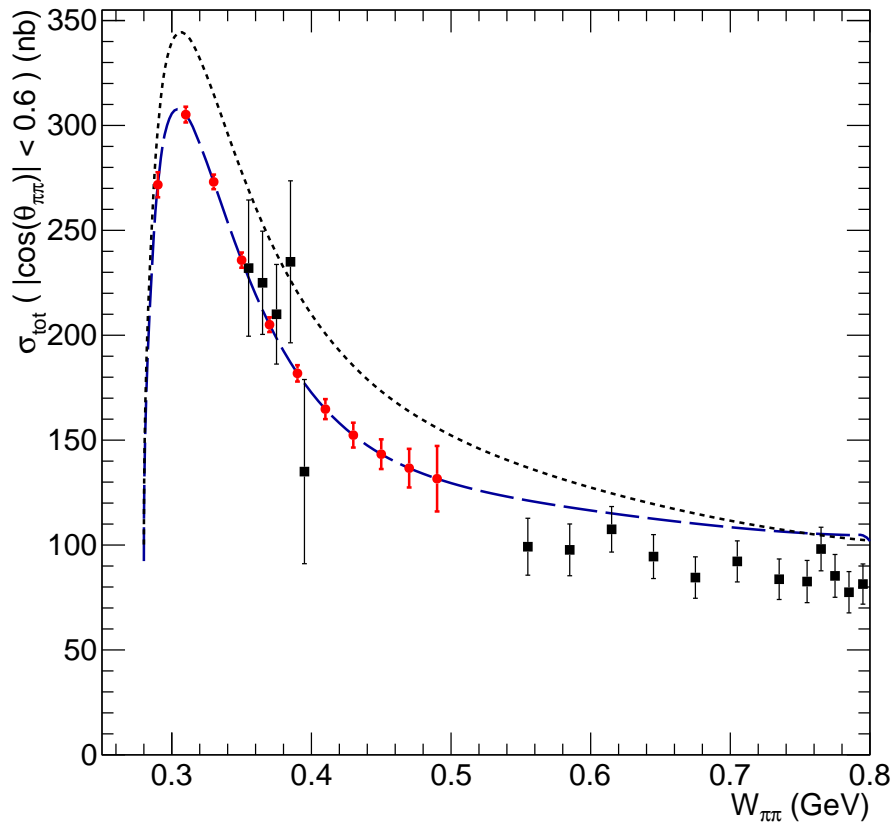


Figure 30: Theory curves for two predicted values of  $\alpha_\pi - \beta_\pi$ , the dashed curve is for 5.7 (ChPT), the dotted curve is for 13.0 (Fil'kov). The black points are published data from the MARK-II measurement. The red points indicate the anticipated statistical errors for the proposed measurement. Error bars are taken from those for the Primakoff fits (red) in Figure 29.

## 6 Summary and beam request

Table 3 summarizes the beam request and experimental requirements for the measurement. 20 days are requested for data production, which will allow the statistical error to be reasonably below the projected systematic error, 0.6% versus 1.5%. There are several non-standard installations required for the running of the experiment: (i) the liquid hydrogen target will be removed, and a solid target installed near the upstream entrance of the magnet, (ii) the muon system will be installed and calibrated, and (iii) it is likely that the experiment will require a customized trigger configuration due to the limited response of FCAL for charged pions. Five running days are requested for the calibration of the muon chambers and testing of the DAQ electronics and trigger.

Table 3: Beam request and running conditions.

Running condition	
Days for production running	20
Days for calibrations	5
Target	$^{116}\text{Sn}$
Photon intensity in coherent peak	$10^7$ photons/s
Edge of coherent peak	6 GeV

## A Muon Detector

In this section we describe a conceptual design for a detector, located behind the FCAL, for positive identification of muons, and to assist FCAL in the identification of charged pions. The relative size and position of this detector are shown in Fig. 17. As described previously in Section 5.5, the production of muon pairs in the kinematic region of interest is approximately five times larger than pion pairs and because the pion and muon masses are similar, the kinematics of the two samples are very similar. We therefore need positive muon identification, which is not part of the nominal GlueX apparatus. The goal of this detector is to be able to tag muons so that they do not contaminate our sample of pion pairs and also to analyze them separately so they can be used as a normalization of pion pair production.

The detector consists of two sets of multi-wire proportional chambers (MWPC<sub>1</sub> and MWPC<sub>2</sub>) separated by approximately 60 cm ( $3\lambda_I$ ) of passive iron absorber (see Fig. 31). Each set of chambers consists of three wire planes, e.g. X-Y-U configuration, to be able to count the number of charged tracks with high efficiency. Muons will be able to penetrate the iron absorber and pions will interact before reaching MWPC<sub>2</sub>. The nuclear interaction length of the lead glass is  $\lambda_I=38$  cm, so the thickness of the FCAL in pion interaction lengths is  $1.2\lambda$ .

The energy sum for each pion event will be 5.5 GeV because of the coherency condition. Extrapolating pion data from the CDHS collaboration, shown in Fig. 32, shows that we can expect approximately 15 charged particles in MWPC<sub>1</sub>. The particle count in MWPC<sub>1</sub> can be used to tag the event as a  $\pi\pi$  event.

Fig. 33 shows that shower leakage as a function of hadron interaction length. At  $4\lambda_I$  the leakage is small, but not negligible. By counting shower particles in MWPC<sub>2</sub> these “punch-through” events can be tagged as pions.

Approximately 4% of the pions will decay before they interact in the FCAL or iron absorber and will be tagged as muons. These decays will limit the certainty with which we can identify pions produced at the target. The overall confidence we can assign to a particular event that it is a pion event when the muon detector has identified two charged particles as such can be computed by applying Bayes’ theorem sequentially

$$P(\pi|1) = \frac{\epsilon \cdot \sigma_\pi}{P(1)} \quad (15)$$

$$P(1) = \epsilon \cdot \sigma_\pi + \alpha \cdot \sigma_\mu \quad (16)$$

$$P(\pi|2) = \frac{\epsilon \cdot P(\pi|1)}{P(2)} \quad (17)$$

$$P(2) = \epsilon \cdot P(\pi|1) + \alpha \cdot (1 - P(\pi|1)), \quad (18)$$

where  $P(\pi| i)$  gives the probability that the event is a pion event, given that  $i=1, 2$  tracks are tagged in the muon detector as pions. The prior probabilities for the pion and

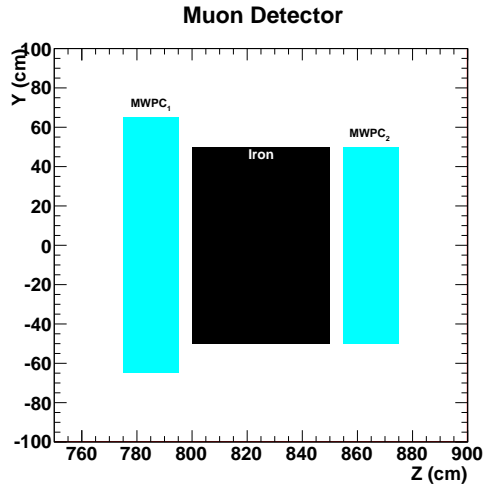


Figure 31: Sketch of muon detector, consisting of a passive iron shield sandwiched between two sets of multi-wire proportional chambers, MWPC<sub>1</sub> and MWPC<sub>2</sub>. The optimal transverse dimensions of the chambers are still being evaluated.

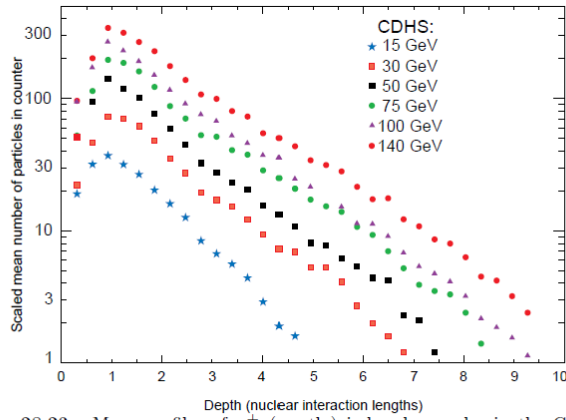


Figure 28.23: Mean profiles of  $\pi^+$  (mostly) induced cascades in the CDHS neutrino detector [143]. See full-color version on color pages at end of book.

Figure 32: Mean profiles of  $\pi^+$  induced cascades in the CDHS neutrino detector.

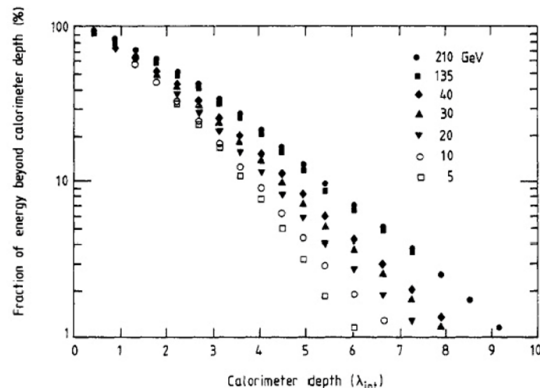


Figure 7. The leakage as a function of the detector depth, for pions of 5–210 GeV, measured in a uranium/plastic-scintillator calorimeter. Data from Catanesi *et al* (1987).

Figure 33: Shower leakage as a function of detector depth for pions.

muons are given by their cross sections, where we assume  $\sigma_{\mu}/\sigma_{\pi} = 10$ . The probability that a particular track is identified as a pion is limited by its decay probability,  $\epsilon$ , and the muon misidentification is specified by  $\alpha$ . The misidentification probability is estimated from the probability for muons multiple-scattering out of the detector acceptance to be about  $\alpha = 0.13\%$ . The probabilities are plotted in Fig. 34. We see that when both tracks are identified as pions, the event probability exceeds 99.998% for the range of pion momenta in our reaction.

The detector is centered on the beamline and should subtend an angle out to  $5.5^{\circ}$  from the target for 95 % acceptance of the pion events. The location of the muon detector must be accommodated on the downstream carriage behind the FCAL detector and its electronic racks. While final dimensions of the detector are yet to be worked out, if the detector is 3 m from the front face of FCAL then its transverse size should be 180 cm. Multiple scattering of a 2.5 GeV muon through FCAL is approximately 20 mrad; if MWPC<sub>1</sub> is at a distance of 2 m from the front face of FCAL, then the projected scatter at the face of the MWPC is 4 cm. This would argue for a MWPC cell spacing of approximately 1 cm.

The thickness of the detector will be approximately 100 cm, taking 20 cm for each the MWPCs and 60 for the iron absorber. These dimensions just barely fit on the platform between the dark box for the FCAL and the electronic racks. In addition, the detector is quite massive (5-10 tons), so a substantial structure would have to be added for support. Also the region down the middle of the platform to the dark room is almost completely blocked, so access may need to be opened by adding stairs on the north and south sides of the platform. Thus it appears the detector can be added to

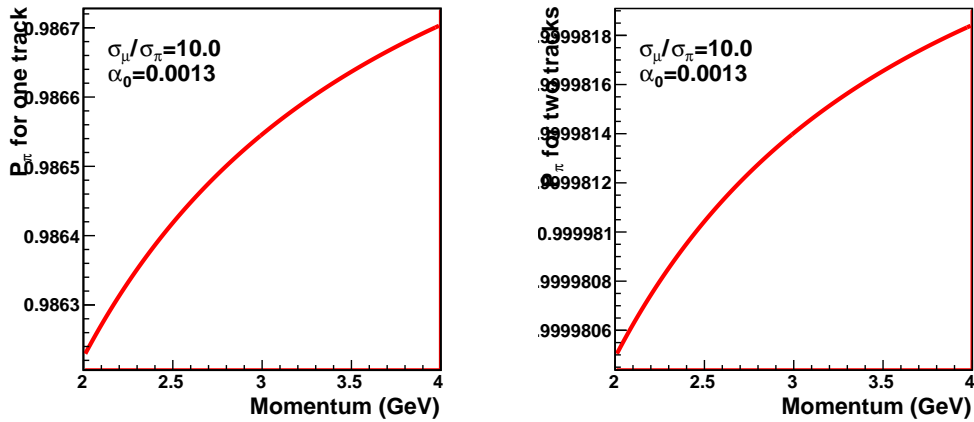


Figure 34: Probability that an event is a pion event, when the muon detector tags one particle as a pion (left plot), and when the muon detector tags both tracks as pions (right plot). The prior probabilities for the pion and muon are assumed to be proportional to their cross sections, where the muon cross section is a factor of ten larger than for pion production.

the existing setup, but a detailed design needs to be completed and properly integrated into the existing infrastructure.

To conclude, the proposed muon detector will identify pion pairs with a 99% probability over the kinematics of interest, and identify muon pairs with even higher probability. We note that the pion decays, which limit the determination of tracks as pions originating from the target, can also be calculated quite accurately. Therefore, with this system in place, the experiment will easily be able to meet its goal of selecting high purity samples of pion and muon pairs.

## References

- [Ah05] J. Ahrens *et al.*, Eur. Phys. J. A23, 113 (2005).  
[Al70] H. Alvensleben *et al.*, Phys. Rev. Lett. 24, 786 (1970).  
[An83] Yu. M. Antipov *et al.*, Phys. Lett. B121, 445 (1983).  
[Aph03] L. Aphecetche *et al.*, NIMA 499, 521-536 (2003)  
[As67] J. Asbury *et al.*, Phys. Rev. Lett. 19, 865 (1967)  
[Aut97] D. Autiero *et al.*, NIMA V387, 352-364 (1997)  
[Ava98] H. Avakian *et al.*, NIMA V417 69-78 (1998)  
[Ba72] J. Ballam, *et al.*, Phys Rev D 5, 545 (1972).  
[Ba92] D. Babusci, *et al.* Phys. Lett. B 277, 158 (1992).  
[Ba08] S. Bakmaev, *et al.*, Phys. Lett. B 660, 494 (2008).  
[Bau90] H. Baumeister *et al.*, NIMA 292, 81-96 (1990)  
[Bo92] J. Boyer *et al.* (MARK-II collaboration), Phys. rev. D 42, 1350 (1990).  
[Br99] J. Bretweg *et al.*, arxiv:hep-ex/9910038v1 (1999).  
[Bu75] V. Budnev, I. Ginzburg, G. Meledin, V. Serbo, Phys. Rep.15, no. 4, 181 (1975).  
[Bu96] U. Burgi, Nucl. Phys. B479, 392 (1996)  
[By09] M. Bychkov *et al.*, Phys. Rev. Lett., 103, 051802 (2009).  
[Do93] J. F. Donoghue and B. R. Holstein, Phys. Rev. D 48, 137 (1993).  
[En12] K. Engel, H. Patel, M. Ramsey-Musolf, arXiv:1201.0809v2 [hep-ph]  
[Fi06] L.V. Fil'kov and V.L. Kashevarov, Phys. Rev. C 73, 035210 (2006).  
[Fr13] J. Friedrich, [http://wwwcompass.cern.ch/compass/publications/talks/t2013/friedrich\\_bormio2013.pdf](http://wwwcompass.cern.ch/compass/publications/talks/t2013/friedrich_bormio2013.pdf)  
[Ga84] J. Gasser and H. Leutwyler, Ann. Phys. 158, 142 (1984).  
[Ga06] J. Gasser, M.A. Ivanov, and M. E. Sainio, Nucl. Phys. B745, 84 (2006).  
[Gl61] V. Glaser, and R. A. Ferrell, Phys. Rev. 121, 886 (1961).  
[Ha66] A. Halprin, C. anderson, H.Primakoff, Phys. Rev. 152, 1295 (1966).  
[Ho90] B. Holstein, Comm. Nucl. Part. Phys. 19, 221 (1990)  
[Ho92] B. Holstein, Nucl. Phys. A546, 213 (1992).  
[Jo13] R. Jones, private communication (2013).  
[Ko08] A. Korchin, PRIMEX note 63 (2008)  
[Mi11] R. Miskimen, Ann. Rev. Nucl. Part. Sci. 61, 1(2011).  
[Mo87] D. Morgan and M.R. Pennington, Phys. Lett. B 192 (1987).  
[Pa08] B. Pasquini, D. Drechsel, and S. Scherer, Phys. Rev. C 77, 06521 (2008).  
[La11] I. Larin, et al., Phys. Rev. Lett. 106, 162303 (2011).  
[Ro] T. Rodrigues, private communication  
[Somov1043] A. Somov, GlueX-doc-1043  
[St71] L. Stodolsky, Phys. Rev. Lett. 26, 404 (1971).  
[Te08] A. Teymurazyan, PhD thesis, Univ. Kentucky (2008).  
[We71] J. Wess and B. Zumino, Phys. Lett. 37B, 422 (1971), and E. Witten, Nucl. Phys. B223, 422 (1983).